

A1
W34m
NO. S-71-6

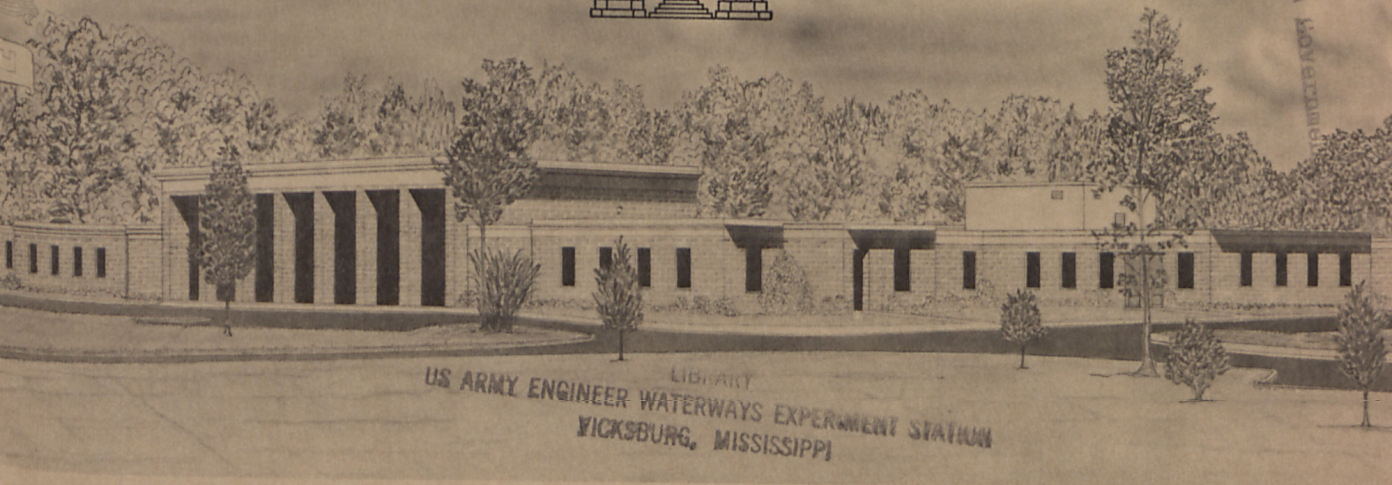


MISCELLANEOUS PAPER S-71-6

FREE-FIELD CODE PREDICTIONS VERSUS FIELD MEASUREMENTS: A COMPARATIVE ANALYSIS FOR THE PRAIRIE FLAT EVENT

by

J. S. Zelasko, G. Y. Baladi



LIBRARY
US ARMY ENGINEER WATERWAYS EXPERIMENT STATION
VICKSBURG, MISSISSIPPI

March 1971

Sponsored by **Defense Atomic Support Agency**

Conducted by **U. S. Army Engineer Waterways Experiment Station, Vicksburg, Mississippi**



MISCELLANEOUS PAPER S-71-6

FREE-FIELD CODE PREDICTIONS VERSUS FIELD MEASUREMENTS: A COMPARATIVE ANALYSIS FOR THE PRAIRIE FLAT EVENT

by

J. S. Zelasko, G. Y. Baladi



March 1971

Sponsored by **Defense Atomic Support Agency**

Subtask SB209

Conducted by **U. S. Army Engineer Waterways Experiment Station, Vicksburg, Mississippi**

ARMY-MRC VICKSBURG, MISS.

This document has been approved for public release and sale; its distribution is unlimited

ABSTRACT

This report documents the results of an airblast-induced ground-shock calculation performed at the U. S. Army Engineer Waterways Experiment Station (WES) for the Operation Prairie Flat 500-ton high-explosive (HE) event. A WES-modified version of the 2D axisymmetric LAYER Code developed by the Paul Weidlinger firm was used for the investigation. Each layer of the soil profile was mathematically modeled with a nonlinear elastic-plastic-compacting type constitutive model that provided good fits to the available material property test data. Field airblast measurements were used to develop an airblast routine suitable for code input. The code results, carried to 300 msec of real time, showed good quantitative and qualitative agreement with the field ground-motion measurements in regions outside the crater zone.

The calculations reported herein represent initial efforts at WES to conduct comprehensive parametric studies of the effectiveness of contemporary mathematical constitutive models in predicting airblast-induced ground motions for several high-explosive field tests. The overall research program includes study of the influences of computational details such as boundary conditions, grid size, and time step and comparative analyses of the calculated ground motions and those recorded during the field test events.

PREFACE

This report was prepared for presentation at the Eric H. Wang Symposium on Protective Structures Technology held at the Air Force Weapons Laboratory, Kirtland Air Force Base, New Mexico, 21-23 July 1970.

The calculations and analyses reported herein were performed for the Defense Atomic Support Agency under Subtask SB209, "Propagation of Ground Shock Through Earth Media," by personnel of the Soils Division, U. S. Army Engineer Waterways Experiment Station (WES). In addition to the authors, Dr. J. S. Zelasko and Dr. G. Y. Baladi, other engineers actively engaged in this study were Mr. J. G. Jackson, Jr., Dr. N. Rhadakrishnan, and PFC B. R. Phillips.

The work was accomplished under the general supervision of Messrs. J. P. Sale and R. G. Ahlvin, Chief and Assistant Chief, respectively, WES Soils Division, and Mr. R. W. Cunny, Chief, Soil Dynamics Branch.

Directors of the WES during the preparation and publication of this report were COL Levi A. Brown, CE, and COL Ernest D. Peixotto, CE. Technical Director was Mr. F. R. Brown.

CONTENTS

| | |
|---|----|
| ABSTRACT----- | 3 |
| PREFACE----- | 4 |
| CONVERSION FACTORS, BRITISH TO METRIC UNITS OF MEASUREMENT----- | 8 |
| CHAPTER 1 INTRODUCTION----- | 9 |
| 1.1 Background----- | 9 |
| 1.2 Purpose and Scope----- | 10 |
| CHAPTER 2 CONSTITUTIVE MODEL DESCRIPTION----- | 11 |
| 2.1 Material Model Parameters----- | 11 |
| 2.2 Representative Soil Properties and Model Construction Procedures----- | 14 |
| 2.3 Model Fits----- | 15 |
| CHAPTER 3 COMPUTATION DETAILS----- | 37 |
| 3.1 Coded Problem----- | 37 |
| 3.2 Air Overpressure Function----- | 37 |
| CHAPTER 4 RESULTS----- | 43 |
| 4.1 General----- | 43 |
| 4.2 Preliminary Code Studies----- | 43 |
| 4.3 Vertical Motions----- | 45 |
| 4.4 Radial Motions----- | 47 |
| CHAPTER 5 CONCLUSIONS AND RECOMMENDATIONS----- | 61 |
| REFERENCES----- | 62 |
| TABLES | |
| 2.1 Material Model Description----- | 18 |
| 3.1 Surface Overpressure Function Parameters----- | 40 |
| FIGURES | |
| 2.1 Compacting hydrostat----- | 19 |
| 2.2 Yield condition----- | 20 |
| 2.3 Types of representative uniaxial strain material property test data supplied for constitutive model analyses----- | 21 |
| 2.4 Comparison of representative dynamic uniaxial strain relations to 2,000 psi with model fit; Zone 1, Prairie Flat----- | 22 |
| 2.5 Comparison of representative dynamic uniaxial strain relations to 500 psi with model fit; Zone 1, Prairie Flat----- | 23 |

| | | |
|------|--|----|
| 2.6 | Comparison of representative dynamic stress paths in uniaxial strain with model fit; unloading from vertical stress levels of 1,000 and 2,000 psi; Zone 1, Prairie Flat----- | 24 |
| 2.7 | Comparison of representative dynamic stress paths in uniaxial strain with model fit; unloading from vertical stress levels of 250 and 500 psi; Zone 1, Prairie Flat---- | 25 |
| 2.8 | Comparison of representative dynamic uniaxial strain relations with model fit; Zone 2, Prairie Flat----- | 26 |
| 2.9 | Comparison of representative dynamic stress paths in uniaxial strain with model fit; Zone 2, Prairie Flat----- | 27 |
| 2.10 | Comparison of representative dynamic uniaxial strain relations with model fit; Zone 3, Prairie Flat----- | 28 |
| 2.11 | Comparison of representative dynamic stress paths in uniaxial strain with model fit; Zone 3, Prairie Flat----- | 29 |
| 2.12 | Comparison of representative dynamic uniaxial strain relations with model fit; Zone 4, Prairie Flat----- | 30 |
| 2.13 | Comparison of representative dynamic stress paths in uniaxial strain with model fit; Zone 4, Prairie Flat----- | 31 |
| 2.14 | Comparison of representative dynamic uniaxial strain relations with model fit; Zones 5 and 6, Prairie Flat---- | 32 |
| 2.15 | Comparison of representative dynamic stress paths in uniaxial strain with model fit; Zone 5, Prairie Flat----- | 33 |
| 2.16 | Comparison of representative dynamic stress paths in uniaxial strain with model fit; Zone 6, Prairie Flat----- | 34 |
| 2.17 | Variation of initial dynamic constrained modulus with depth; Prairie Flat----- | 35 |
| 2.18 | Comparison of representative dynamic shear strength properties, Zones 1 through 6, Prairie Flat----- | 36 |
| 3.1 | Schematic representation of coded Prairie Flat boundary value problem----- | 41 |
| 3.2 | Comparison of mathematical fit with Prairie Flat air overpressure measurements at selected ground ranges----- | 42 |
| 4.1 | Results of grid-size parameter study at 800-psi contour-- | 49 |
| 4.2 | Comparison of computed vertical particle velocity waveforms with field measurements; range 220 feet; Prairie Flat----- | 50 |
| 4.3 | Comparison of computed vertical particle velocity waveforms with field measurements; range 330 feet; Prairie Flat----- | 51 |
| 4.4 | Comparison of computed vertical displacement waveforms with field measurements; range 220 feet; Prairie Flat---- | 52 |
| 4.5 | Comparison of computed vertical displacement waveforms with field measurements; range 330 feet; Prairie Flat---- | 53 |
| 4.6 | Comparison of measured and computed peak vertical particle velocity and displacement attenuations versus depth; range 220 feet; Prairie Flat----- | 54 |

| | | |
|------|---|-----|
| 4.7 | Comparison of measured and computed peak vertical particle velocity and displacement attenuations versus depth; range 330 feet; Prairie Flat----- | 55 |
| 4.8 | Computed attenuations of peak stress; ranges 220 and 330 feet; Prairie Flat----- | 56 |
| 4.9 | Comparison of computed radial particle velocity waveforms with field measurements; range 220 feet; Prairie Flat----- | 57. |
| 4.10 | Comparison of computed radial particle velocity waveforms with field measurements; range 330 feet; Prairie Flat----- | 58 |
| 4.11 | Comparison of computed radial displacement waveforms with field measurements; range 220 feet; Prairie Flat---- | 59 |
| 4.12 | Comparison of computed radial displacement waveforms with field measurements; range 330 feet; Prairie Flat---- | 60 |

• CONVERSION FACTORS, BRITISH TO METRIC UNITS OF MEASUREMENT

British units of measurement used in this report can be converted to metric units as follows.

| Multiply | By | To Obtain |
|------------------------|----------|---------------------------------|
| inches | 2.54 | centimeters |
| feet | 0.3048 | meters |
| tons (2,000 pounds) | 907.185 | kilograms |
| pounds per square inch | 0.070307 | kilograms per square centimeter |
| kips per square inch | 70.307 | kilograms per square centimeter |
| pounds per cubic foot | 16.0185 | kilograms per cubic meter |

CHAPTER 1

INTRODUCTION

1.1 BACKGROUND

The state-of-the-art in constitutive modeling of earth materials for free-field ground-shock calculation purposes is continually being upgraded to incorporate new developments both in theory and material property evaluation. As a consequence, each new major calculation project is usually performed with a supposedly improved model of the pertinent site materials. However, very little research effort has been devoted to an assessment of the degree of improvement, if any, that the newer models actually provide. This information gap is currently of concern to theoreticians and experimentalists alike, since a number of serious objections have recently been raised to the continued use of many contemporary models.

Under sponsorship of the Defense Atomic Support Agency (DASA), the U. S. Army Engineer Waterways Experiment Station (WES) has recently initiated a program to evaluate a variety of contemporary constitutive models by performing parametric code calculations against well-documented field test events. Operation Prairie Flat, a 500-ton¹ high-explosive (HE) event executed 9 August 1968 (Reference 1) at the Watching Hill Test Range, Suffield, Alberta, Canada, was the first event chosen for study in this research program.

Nonlinear elastic-plastic-compacting (NEPC) models have been the mainstay of the code community during the past few years. As implied by their name, these models exhibit behavior defined by elasticity and theory of perfect plasticity, as well as compaction behavior; the

¹ A table of factors for converting British units of measurement to metric units is presented on page 8.

latter mechanism predicts mechanical hysteresis during a cycle of virgin loading and unloading through subyield stress paths. In general, the NEPC models are prescribed by specification of a plastic yield criterion and flow rule, a nonlinear compacting hydrostat, and one other elastic parameter such as Poisson's ratio ν or shear modulus G . Both ν and G have recently seen wide service formulated either as functions of the first stress invariant or as constants. The first model chosen for the calculation study was a mixed constant ν -constant G NEPC model. This model, called the hybrid ν - G , is a recent innovation resulting from WES collaboration with Applied Theory, Inc., on a Minuteman study sponsored by the Air Force Space and Missile Systems Organization.

To date, one large two-dimensional (2D) calculation, using the hybrid ν - G model, has been carried out to a real time of 300 msec. A mathematical idealization of the Prairie Flat surface overpressure history between the nominal 1500- and 40-psi contours (range = 84 and 560 feet, respectively) was developed at WES for this purpose. The code used for this effort was a WES-modified version of the Weidlinger axisymmetric LAYER Code (Reference 2) adapted for use on an accessible GE-635 computer.

1.2 PURPOSE AND SCOPE

The primary purpose of this report is to document a code-based analysis of the Prairie Flat ground motions at intermediate ranges.

The material model and the mathematical fits to representative Prairie Flat soil properties for six idealized layers are described in Chapter 2. Details of the coded problem and the mathematical airblast routine are contained in Chapter 3. In Chapter 4, the code results are compared with field measurements at selected intermediate ground ranges and an analysis of the event up to 300 msec from detonation is presented. Conclusions and recommendations are presented in Chapter 5.

CHAPTER 2

CONSTITUTIVE MODEL DESCRIPTION

2.1 MATERIAL MODEL PARAMETERS

The material hydrostat is shown in Figure 2.1. Changes in dynamic mean normal stress P_{dyn} and volumetric strain ϵ_{kk} are defined by three polynomial functions:

$$P_{\ell} = P_g + \sum_{n=1}^m A_n (\epsilon_{\text{max}})^n \quad (1)$$

$$P_u = P_g + \sum_{n=1}^m B_n (\epsilon_{kk} - \epsilon_s)^n, \quad \epsilon_s < \epsilon_{kk} \leq \epsilon_{\text{max}} \quad (2)$$

$$\epsilon_s = \sum_{n=1}^m C_n (\epsilon_{\text{max}})^n \quad (3)$$

where: P_{ℓ} and P_u = total (static plus dynamic) mean normal stresses on the loading and unloading hydrostats, respectively

P_g = static mean normal overburden stress¹

¹

$$P_g = \int_0^Z \frac{\gamma_i [1 + 2\nu_i / (1 - \nu_i)]}{3} dz$$

where: γ_i = wet unit weight of i^{th} layer.

ν_i = initial static Poisson's ratio of the i^{th} layer (not necessarily = initial dynamic ν). For the calculations reported herein $\nu_i = 0.5$ was assumed for each layer.

Z = depth coordinate.

ϵ_{\max} = maximum volumetric strain achieved

ϵ_s = permanent set relative to a closed cycle of
dynamic mean normal stress change

A_n , B_n , and C_n = material coefficients

When $\epsilon_{kk} < \epsilon_s$, P_u is computed from

$$P_u = P_g + B_1(\epsilon_{kk} - \epsilon_s) \quad (4)$$

where: B_1 = slope of the unloading hydrostat at zero dynamic mean normal stress.

Equations 1, 2, and 4 determine the slopes of the hydrostat to be unique functions of mean normal stress. To avoid energy generation problems, at any given mean normal stress level

$$\frac{dP_\ell}{d\epsilon_{kk}} \leq \frac{dP_u}{d\epsilon_{kk}} \quad (5)$$

The material is assumed to be fractured for stress states $P_u \leq 0$ (soils exhibit little or no tensile strength); when this occurs, P_u and each individual deviator stress are set equal to zero.

The hybrid v-G model is initially a constant Poisson's ratio NEPC model during virgin loading. Therefore, the loading shear modulus can be obtained from the slope of the loading hydrostat by

$$G_\ell = \frac{3(1 - 2\nu_\ell)}{2(1 + \nu_\ell)} \cdot \sum_{n=1}^m n A_n (\epsilon_{\max})^{n-1} \quad (6)$$

where: ν_ℓ = loading Poisson's ratio.

However, the value of G computed from Equation 6 is constrained to have a definite upper limit G_{\max} . Thus, at a prescribed mean normal

stress level, virgin loading switches to a constant-G ($G_\ell = G_{\max}$) NEPC model.

The unloading shear modulus is a constant for a given cycle of unloading-reloading, but the value of the constant is a function of the maximum mean normal stress, i.e.

$$G_u = f(P_{\max}) \quad (7)$$

Therefore, the unloading shear modulus can be determined from

$$G_u = \frac{3(1 - 2\nu_u)}{2(1 + \nu_u)} \cdot \sum_{n=1}^m n B_n (\epsilon_{\max} - \epsilon_s)^{n-1} \quad (8)$$

where: ν_u = unloading Poisson's ratio (a constant).

In general, $\nu_u \neq \nu_\ell$. The value of G computed from Equation 8 is also constrained by G_{\max} . Thus, according to Equation 5, at any mean normal stress level,

$$G_\ell \leq G_u \leq G_{\max} \quad (9)$$

Equations 5 and 9 state that the material can exhibit hysteresis in shear as well as in compression for all virgin loading cycles. Equations 5, 6, 8, and 9 specify that the material cannot, under any circumstances, generate energy.

The material description is completed by specification of a failure, or yield, surface and a flow rule. In order to realistically match typical soil shear strength data, a modified form of the yield function proposed by Drucker and Prager (Reference 3) was adopted. This form, widely accepted in recent years by all major calculators, is

written as a polynomial function of dynamic mean normal stress (Figure 2.2)

$$\sqrt{J_2'} = \sum_{n=1}^m D_n (P_{\text{dyn}})^{n-1} \quad (10)$$

where: J_2' = second invariant of the stress deviator tensor.

At low stress levels the material exhibits Coulomb type yield behavior, but transitions into Von Mises behavior at higher stresses. Beyond the point at which the slope of Equation 10 becomes zero ($P_{\text{dyn}} > P_c$, Figure 2.2).

$$\sqrt{J_2'} = \text{Constant} \quad (11)$$

The code calculations reported in this report utilized the Von Mises flow rule. Because the Prairie Flat soils above the groundwater table generally exhibit Coulomb yield behavior, this rule is nonassociative in these materials.

2.2 REPRESENTATIVE SOIL PROPERTIES AND MODEL CONSTRUCTION PROCEDURES

Laboratory material property tests and data analyses for Operation Prairie Flat were accomplished as a separate, though related, task under the DASA nuclear weapons effects research program at WES. The outcome of this task resulted in the division of the Prairie Flat profile into six idealized horizontal layers or zones. The density and depth to bottom of each zone are listed at the top of Table 2.1. For each zone, representative dynamic load-unload stress-strain and stress path relations for uniaxial strain (UX), Figure 2.3, and values of ν_l were made available for constitutive model analyses.

Construction of a constant Poisson's ratio NEPC model, well documented in Reference 4, is a relatively straightforward procedure.

This procedure was used, along with the representative UX stress-strain relations and ν_ℓ values, to construct loading and unloading hydrostats for each of the six zones, assuming the materials possessed nonassociated flow rules. Then, guided by the representative unloading UX stress paths, variations in G_{\max} and ν_u were parametrically studied for each zone. This effort, coordinated with the WES material property testing and data analysis group, eventually led to the selection of representative values of G_{\max} and ν_u . These values are listed along with all other pertinent model parameters for each zone in Table 2.1. NU in the table is ν ; $PC = P_c$; EFFEK is the value of the constant in Equation 11; coefficients A, AM, AU, and AY define the polynomials for the loading hydrostat, the permanent set, the unloading hydrostat, and the yield condition, respectively; GZ and EMZ are the initial shear and constrained moduli, respectively; P-VEL and S-VEL are the initial elastic compression and shear wave speeds; EZ is the initial Young's modulus; and KMAX and EM are irrelevant to this report.

2.3 MODEL FITS

Figure 2.4 compares the representative Zone 1 UX stress-strain relations with the model fits; Figure 2.5 shows the low stress-level fits at an expanded scale. In Figures 2.6 and 2.7 the corresponding Zone 1 stress path comparisons are presented. As an aid to the identification of the stress paths, significant stress states have been labeled; point A defines the intersection of the representative loading path with the yield surface, point 1 defines the model loading path and yield surface intersection, points B and 2, respectively, define representative and model unloading departure states, and points C and 3, respectively, locate the states at which the representative and model unloading paths intersect the lower yield surface.

Figures 2.4 through 2.7 indicate that in Zone 1 good quality fits

were obtained for both types of UX data over the entire stress range considered (0 to 2000 psi); however, because the model incorporates strain-axis translation for the unloading hydrostat, the soft hooks at the bottoms of the UX unloading stress-strain curves could not be matched without creating energy-generation problems in the model.² Comparisons of the representative and modeled UX relations for Zones 2 through 6 are shown in Figures 2.8 through 2.16.

Material behavior within the first three zones is characterized by very low constrained moduli during virgin loading in uniaxial strain and large hysteretic strain energy loss upon unloading due to very high air void contents and low densities. The relation for Zone 4 is somewhat stiffer and less hysteretic due to increased density, increased geostatic overburden confinement, and decreased air void content. This trend continues very sharply into Zone 5 (which underlies the groundwater table³) and culminates in Zone 6 with a condition of full saturation and a constrained loading modulus approximately that of water. The stiffness variations between Zone 1 and 6 differ by almost two orders of magnitude as indicated in Figure 2.17 where the initial constrained modulus has been plotted versus depth.

Shear strength also varies significantly with depth as shown in Figure 2.18. The saturated and nearly saturated materials in the vicinity of the groundwater table exhibit little or no increase in strength with increasing mean normal stress, whereas the upper, high

² Use of an associated flow rule would provide improved agreement with the UX unloading hooks. This is one of the model parameters under consideration for future Prairie Flat calculations.

³ Just prior to the Prairie Flat test, piezometer readings determined a depth to groundwater of approximately 23 feet.

initial air void content materials show large increases in strength with increasing mean normal stress.

TABLE 2.1. MATERIAL MODEL DESCRIPTION

YIELD CONDITION. $SQJ2=AY(1)+SUM(AY(N+1)*P**N)$, $N=1,2,3,...,9$ P.LT.PC
 $SQJ2=EIFK$ P.GT.PC
 PRESSURE .GT.OR.EQ. ZERO
 FLOW RULE - MISES TYPE

PRESSURE - VOLUME RELATION
 INITIAL LOADING. $PHAX(EKK)=SUM(A(N)*EKK**N)$ WHERE, $N=1,2,3,...,10$
 UNLOADING-RELOADING. $P=SUM(AU(N)*DELEKK**N)$ WHERE, $N=1,2,3,...,10$
 $DELEKK=EKK-EPSS(EKKMAX)$
 $EPSS=SUM(AH(N)*EPSMAX**N)$
 LOADING DEVIATOR RELATION $NU=CONST.FOR G LESS THAN GMAX ELSE GL=GMAX$
 UNLOADING DEVIATOR RELATION $GUN=CONSTANT=MIN(GUN(PHAX), GMAX)$

| LAYER | 1 | 2 | 3 | 4 | 5 | 6 |
|--------------|--------------|--------------|--------------|--------------|--------------|--------------|
| DEPTH FT | 0.000 | 12.000 | 18.000 | 24.000 | 33.000 | |
| DENSITY PCF | 92.000 | 94.500 | 106.000 | 117.500 | 121.000 | 121.500 |
| LOAD. NU | 0.3000 | 0.2800 | 0.3200 | 0.3800 | 0.4200 | 0.4700 |
| UNL. NU | 0.3000 | 0.2600 | 0.3000 | 0.3800 | 0.4200 | 0.4700 |
| PC KSI | 2.0000 | 2.0000 | 2.0000 | 1.5000 | 1.5000 | 2.0000 |
| EFFK KSI | 0.2425 | 0.7006 | 0.4042 | 0.1732 | 0.0693 | 0.0346 |
| KMAX KSI | 59.50 | 183.00 | 150.00 | 146.00 | 310.00 | 380.00 |
| GMAX KSI | 9.00 | 40.00 | 35.00 | 30.00 | 20.00 | 15.00 |
| EM | -0.38300E 00 | -0.24200E 00 | -0.25150E 00 | -0.42600E-01 | -0.12800E-01 | -0.18000E-01 |
| A(1) KSI | 0.30080E 01 | 0.23398E 01 | 0.34480E 01 | 0.59419E 01 | 0.16316E 02 | 0.25000E 03 |
| A(2) KSI | -0.11562E 01 | 0.83360E 01 | -0.14274E 02 | -0.47875E 02 | -0.14984E 04 | 0. |
| A(3) KSI | -0.32020E 03 | 0.41024E 02 | 0.14044E 03 | 0.61933E 04 | 0.71679E 05 | 0. |
| A(4) KSI | 0.36878E 04 | -0.86973E 02 | 0.30308E 03 | -0.12220E 06 | 0.14530E 08 | 0. |
| A(5) KSI | -0.16336E 05 | 0. | -0.70059E 04 | 0.11284E 07 | 0.37303E 09 | 0. |
| A(6) KSI | 0.33485E 05 | 0. | 0.35788E 05 | 0. | -0.46792E 09 | 0. |
| A(7) KSI | -0.26230E 05 | 0. | -0.57306E 05 | 0. | 0.80294E 08 | 0. |
| A(8) KSI | 0. | 0. | 0. | 0. | 0. | 0. |
| A(9) KSI | 0. | 0. | 0. | 0. | 0. | 0. |
| A(10) KSI | 0. | 0. | 0. | 0. | 0. | 0. |
| AH(1) | 0.37200E 00 | 0.31309E 00 | 0.43958E 00 | 0.88125E-01 | 0.88537E-01 | 0.16667E 00 |
| AH(2) | -0.89350E 01 | -0.18193E 02 | -0.22345E 02 | -0.11047E 02 | -0.83469E 02 | 0. |
| AH(3) | -0.77051E 02 | -0.35758E 03 | -0.61113E 03 | 0.27731E 04 | 0.51081E 05 | 0. |
| AH(4) | -0.36963E 03 | -0.46706E 04 | -0.10730E 05 | 0.21159E 06 | 0.19733E 08 | 0. |
| AH(5) | -0.10211E 04 | -0.38855E 05 | -0.12252E 06 | 0.67072E 07 | 0.27374E 10 | 0. |
| AH(6) | -0.15176E 04 | -0.19218E 06 | -0.91465E 06 | 0.10439E 09 | 0.17095E 12 | 0. |
| AH(7) | -0.93921E 03 | -0.50766E 06 | -0.44147E 07 | 0.62865E 09 | 0.40282E 13 | 0. |
| AH(8) | 0. | -0.54790E 06 | -0.13241E 08 | 0. | 0. | 0. |
| AH(9) | 0. | 0. | -0.22398E 08 | 0. | 0. | 0. |
| AH(10) | 0. | 0. | -0.16313E 08 | 0. | 0. | 0. |
| AU(1) KSI | 0.63174E 01 | 0.35273E 01 | 0.39054E 01 | 0.65287E 01 | 0.17902E 02 | 0.30000E 03 |
| AU(2) KSI | -0.15134E 03 | 0.51493E 03 | 0.41843E 04 | 0.15548E 03 | 0.40889E 04 | 0. |
| AU(3) KSI | 0.17338E 05 | -0.13374E 06 | -0.13863E 07 | -0.16835E 05 | 0.18888E 07 | 0. |
| AU(4) KSI | -0.25845E 06 | 0.16045E 08 | 0.21699E 09 | 0.94078E 07 | -0.31729E 10 | 0. |
| AU(5) KSI | 0.15320E 07 | -0.58948E 09 | -0.13811E 11 | -0.10800E 10 | 0.13552E 13 | 0. |
| AU(6) KSI | 0. | 0.73389E 10 | 0.39980E 12 | 0.97921E 11 | -0.13531E 15 | 0. |
| AU(7) KSI | 0. | 0.20521E 11 | -0.43591E 13 | 0. | 0. | 0. |
| AU(8) KSI | 0. | 0. | 0. | 0. | 0. | 0. |
| AU(9) KSI | 0. | 0. | 0. | 0. | 0. | 0. |
| AU(10) KSI | 0. | 0. | 0. | 0. | 0. | 0. |
| AY(1) KSI | 0.13447E-01 | 0.12587E-01 | 0.11716E-01 | 0.89651E-02 | 0.80140E-02 | 0.13967E-01 |
| AY(2) | 0.31745E 00 | 0.77450E 00 | 0.43131E 00 | 0.23581E 00 | 0.11016E 00 | 0.26440E-01 |
| AY(3) KSI-1 | -0.18772E 01 | -0.39516E 00 | -0.15336E 00 | -0.11689E 00 | -0.74371E-01 | -0.12465E-01 |
| AY(4) KSI-2 | 0.25273E 01 | 0.89933E-01 | 0.18327E-01 | 0.22436E-01 | 0.19141E-01 | 0.22210E-02 |
| AY(5) KSI-3 | -0.18496E 01 | 0. | 0. | 0. | 0. | 0. |
| AY(6) KSI-4 | 0.68358E 00 | 0. | 0. | 0. | 0. | 0. |
| AY(7) KSI-5 | -0.99964E-01 | 0. | 0. | 0. | 0. | 0. |
| AY(8) KSI-6 | 0. | 0. | 0. | 0. | 0. | 0. |
| AY(9) KSI-7 | 0. | 0. | 0. | 0. | 0. | 0. |
| AY(10) KSI-8 | 0. | 0. | 0. | 0. | 0. | 0. |
| CZ KSI | 1.388 | 1.206 | 1.411 | 1.550 | 2.758 | 15.306 |
| EMZ KSI | 4.859 | 3.948 | 5.329 | 8.089 | 19.993 | 270.488 |
| EZ KSI | 3.610 | 3.089 | 3.724 | 4.278 | 7.832 | 45.000 |
| P-VFL FPS | 494.7 | 440.0 | 482.6 | 561.9 | 874.9 | 3211.1 |
| S-VFL FPS | 264.4 | 243.2 | 248.3 | 247.2 | 324.9 | 764.0 |

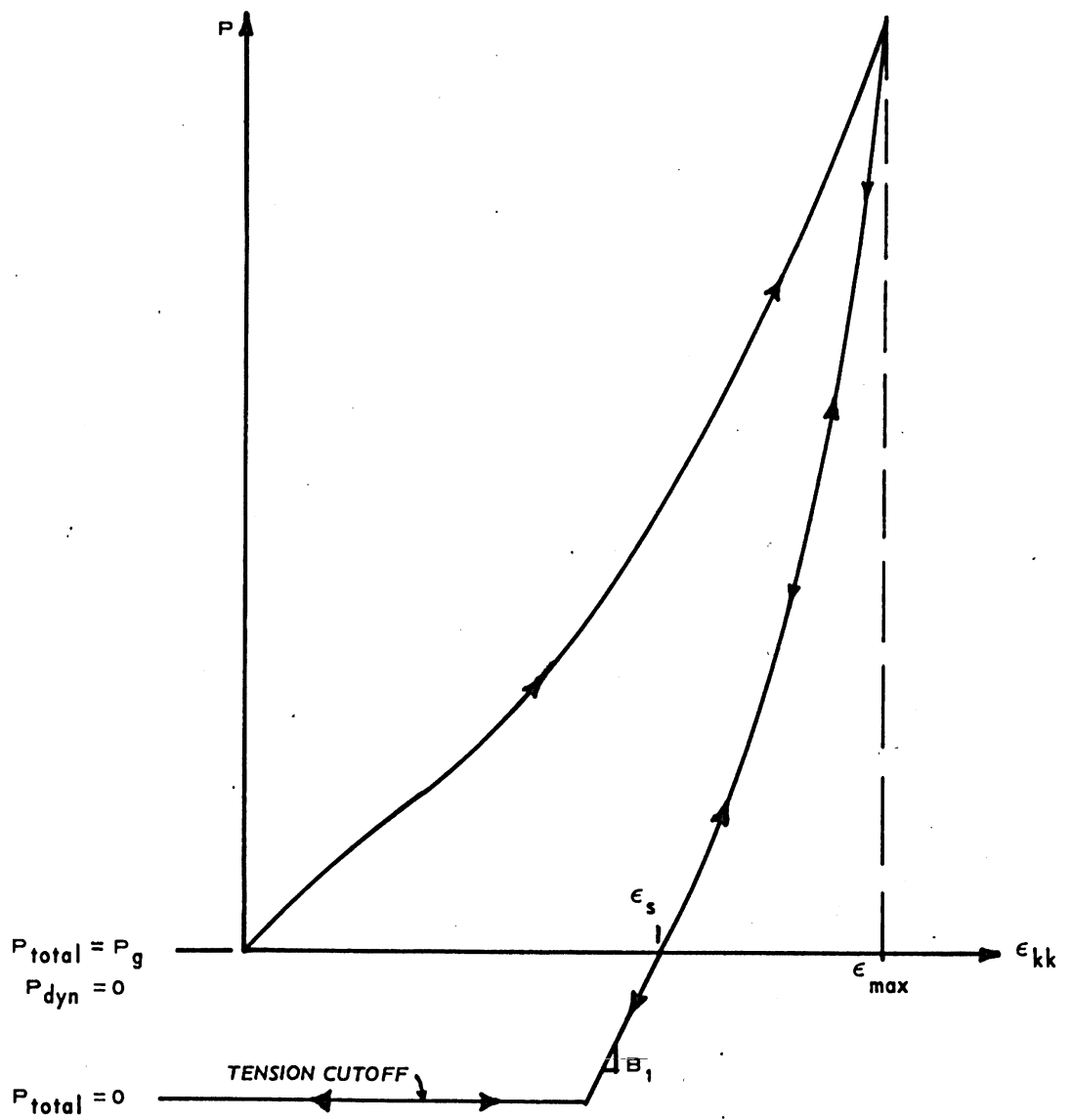


Figure 2.1 Compacting hydrostat.

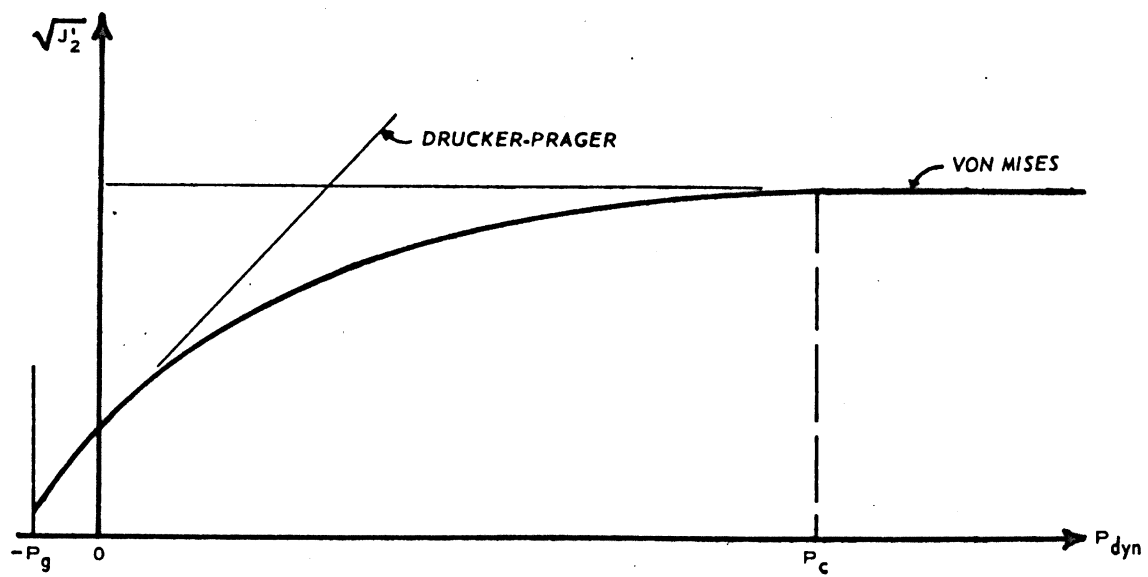
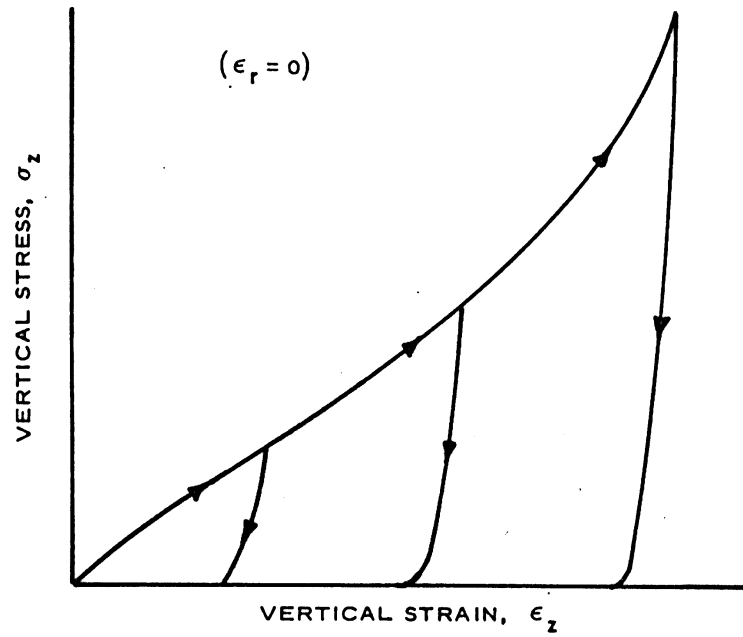


Figure 2.2 Yield condition.

STRESS-STRAIN INFORMATION



STRESS-PATH INFORMATION

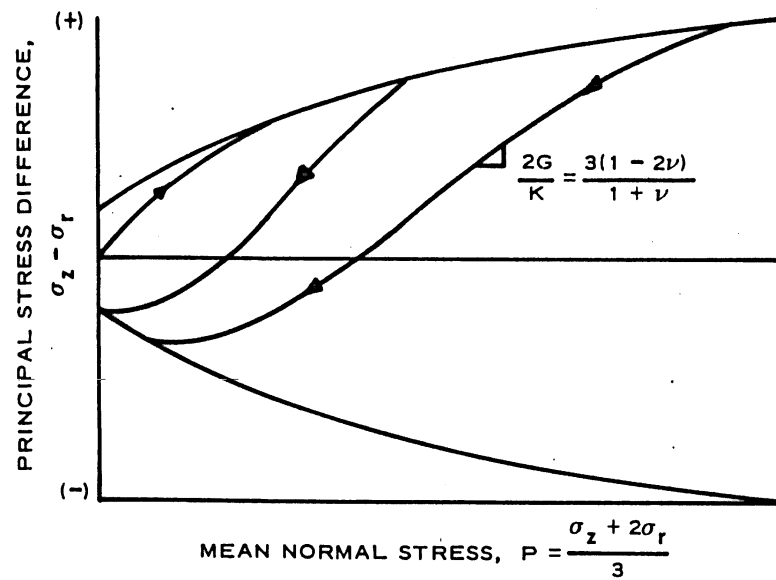


Figure 2.3 Types of representative uniaxial strain material property test data supplied for constitutive model analyses.

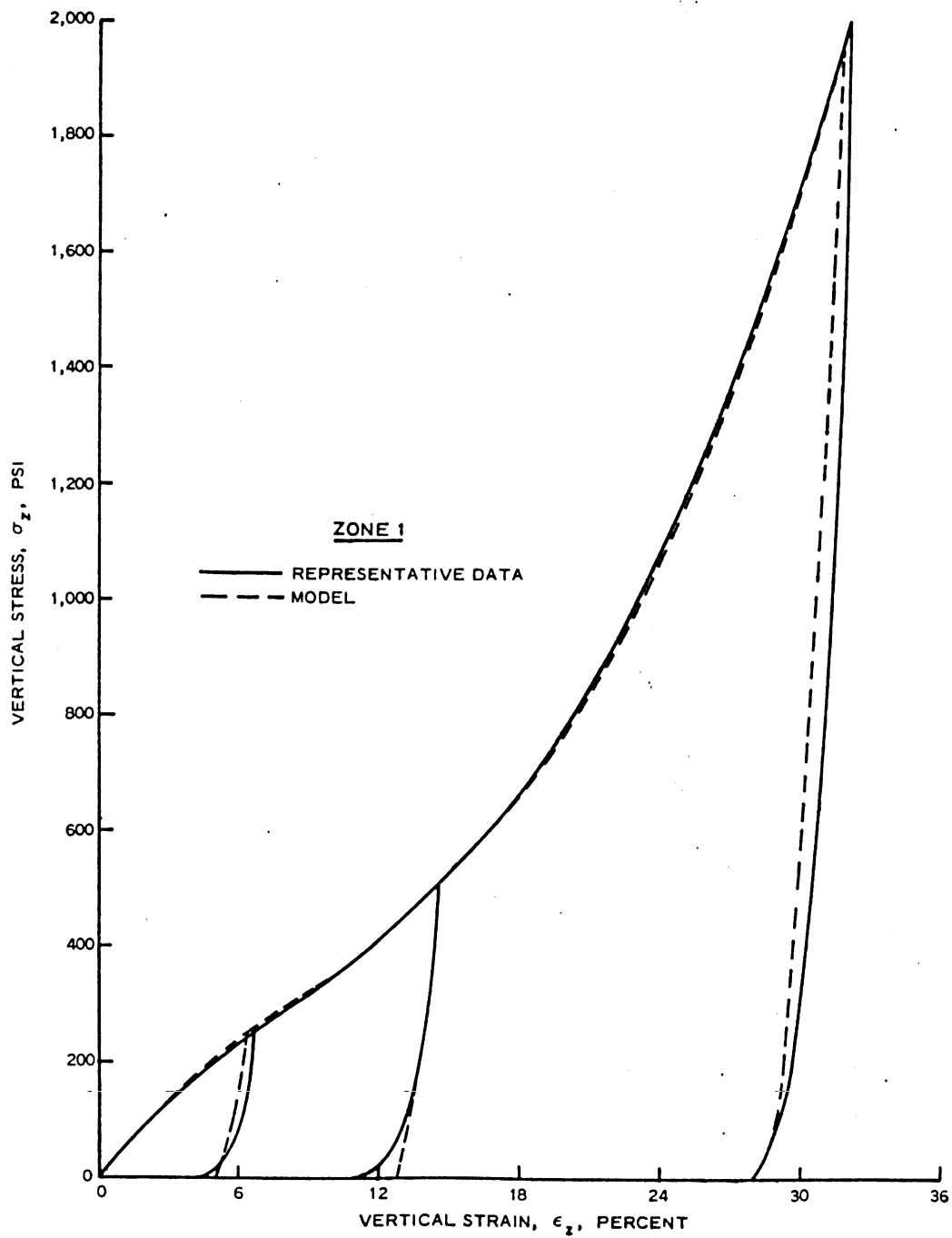


Figure 2.4 Comparison of representative dynamic uniaxial strain relations to 2,000 psi with model fit; Zone 1, Prairie Flat.

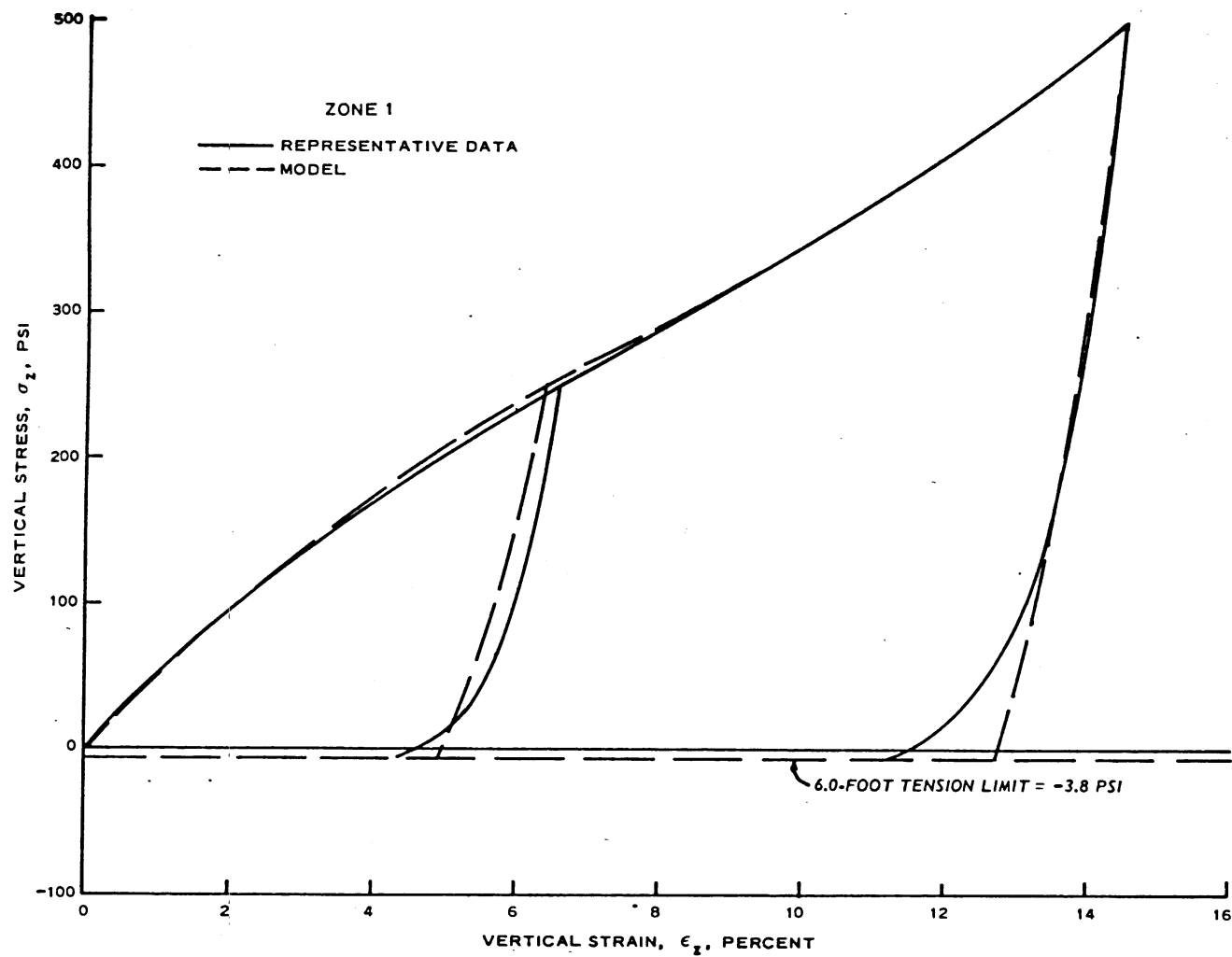


Figure 2.5 Comparison of representative dynamic uniaxial strain relations to 500 psi with model fit; Zone 1, Prairie Flat.

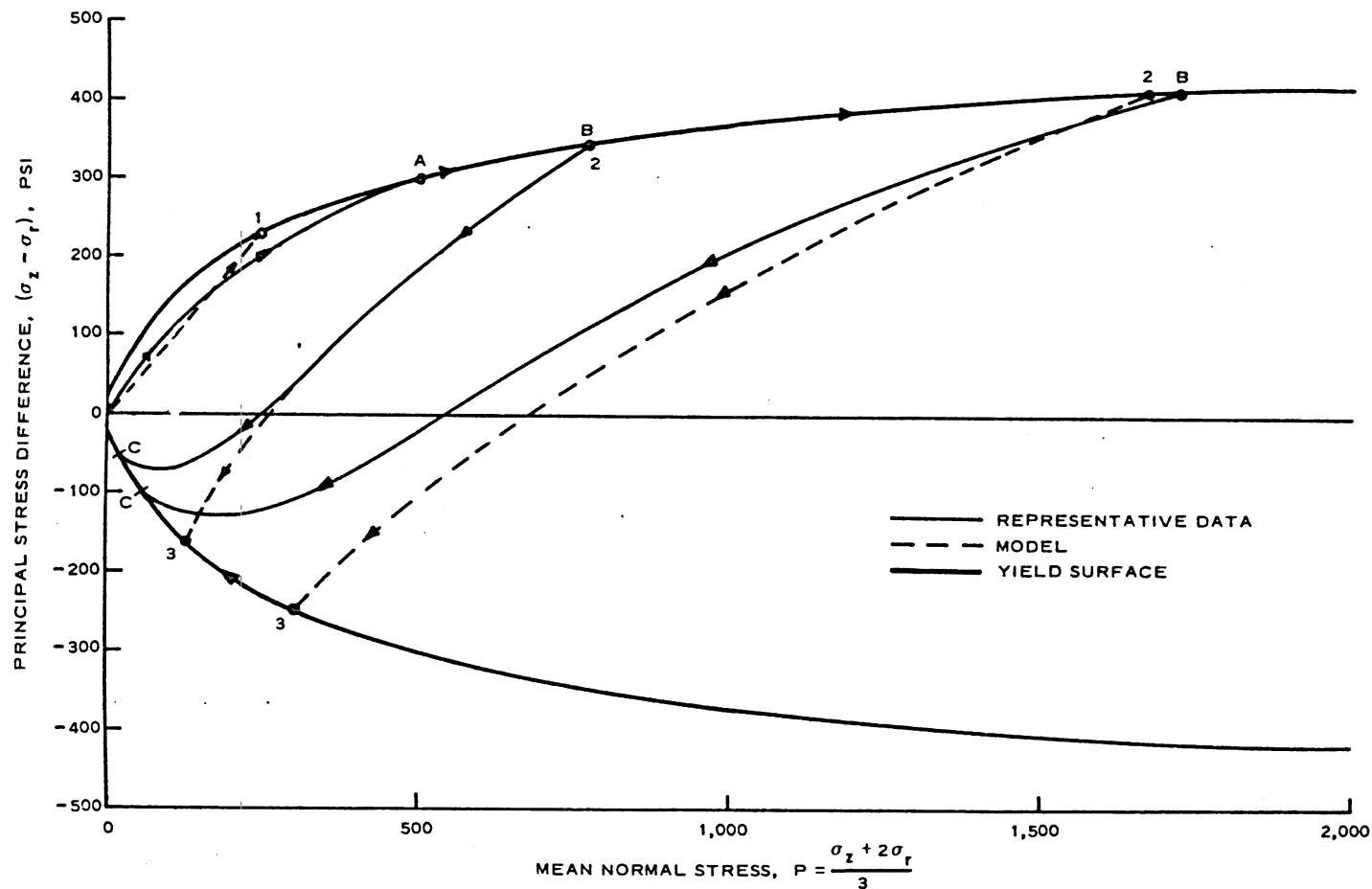


Figure 2.6 Comparison of representative dynamic stress paths in uniaxial strain with model fit; unloading from vertical stress levels of 1,000 and 2,000 psi; Zone 1, Prairie Flat.

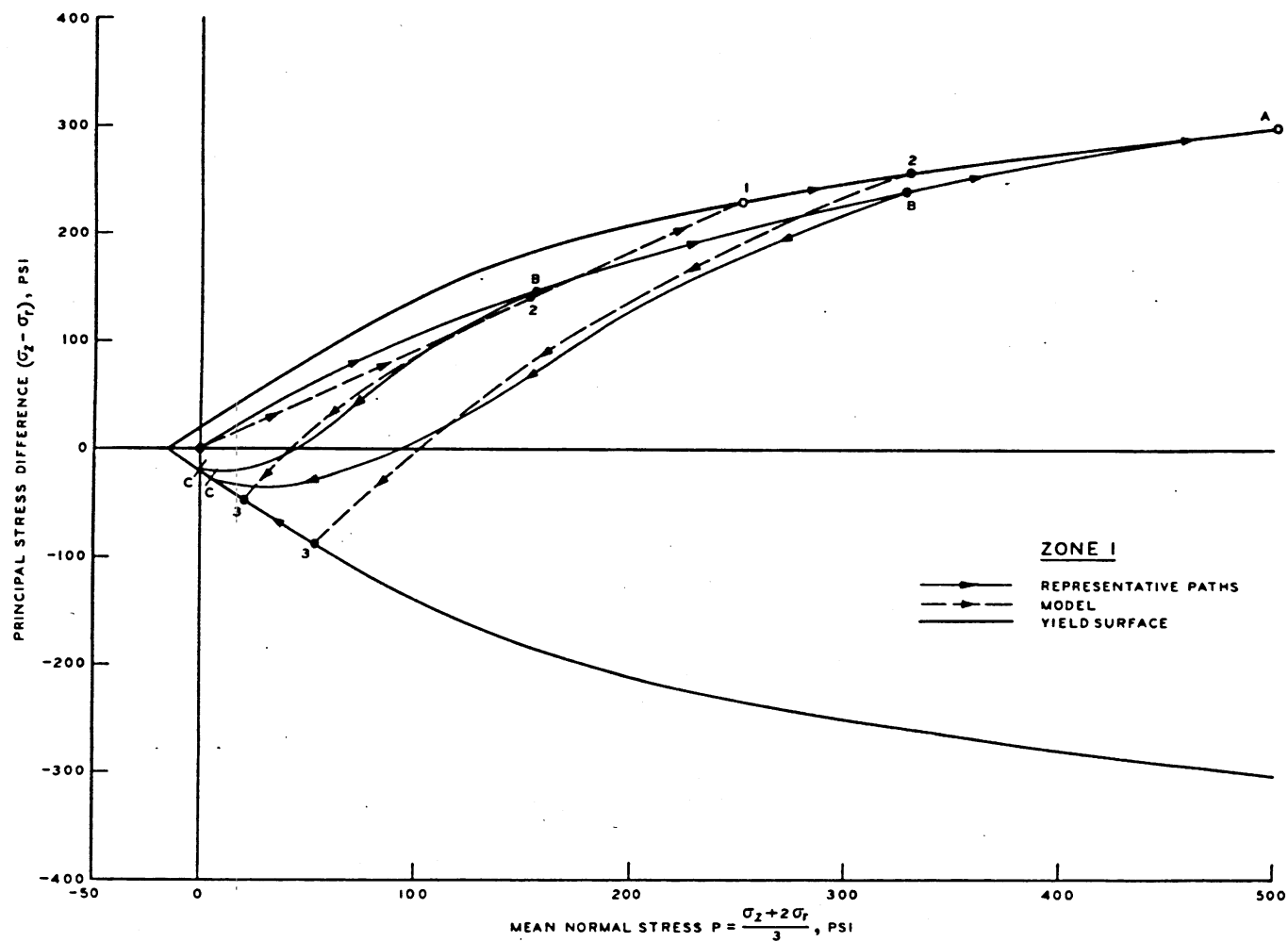


Figure 2.7 Comparison of representative dynamic stress paths in uniaxial strain with model fit; unloading from vertical stress levels of 250 and 500 psi; Zone 1, Prairie Flat.

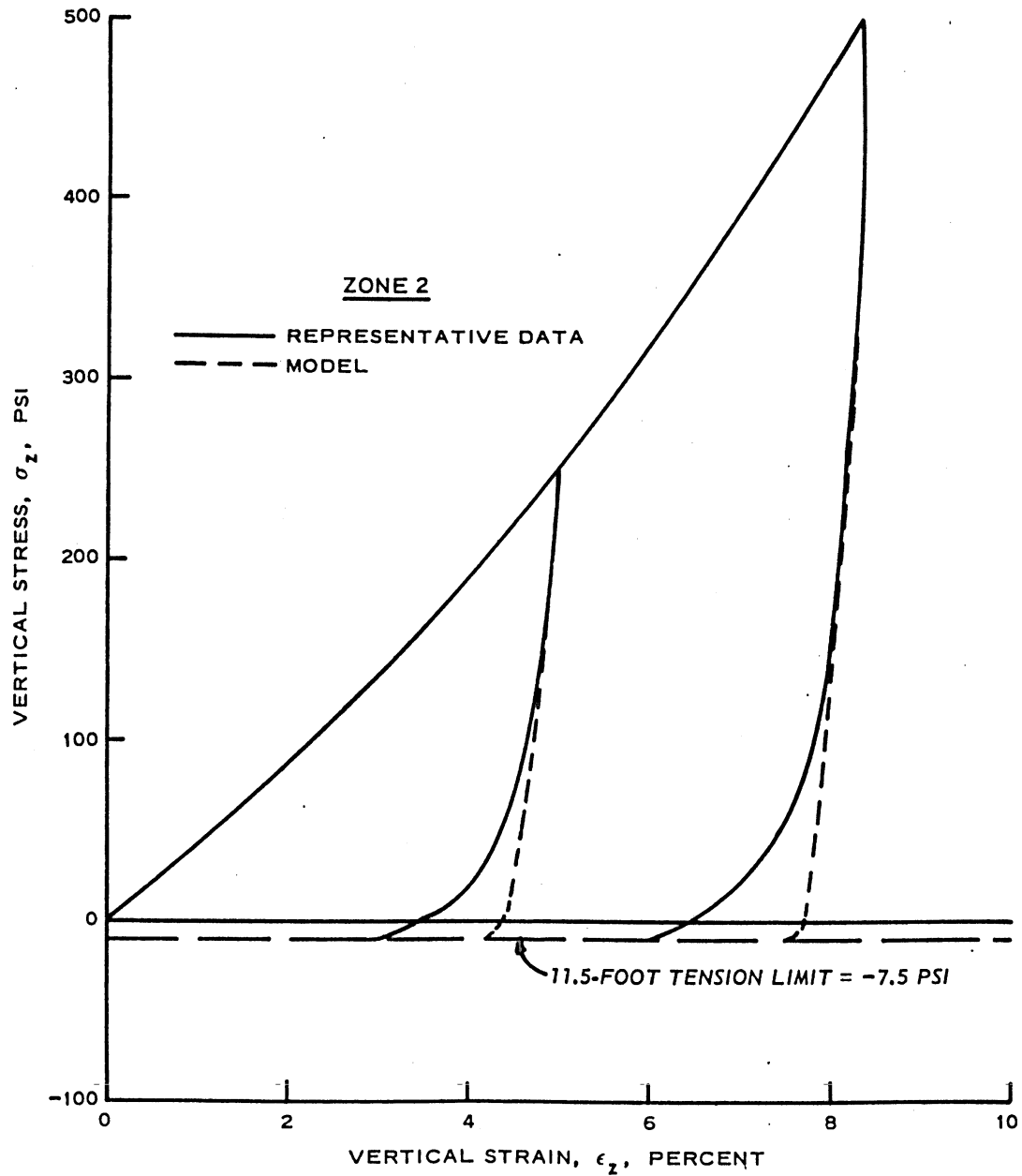


Figure 2.8 Comparison of representative dynamic uniaxial strain relations with model fit; Zone 2, Prairie Flat.

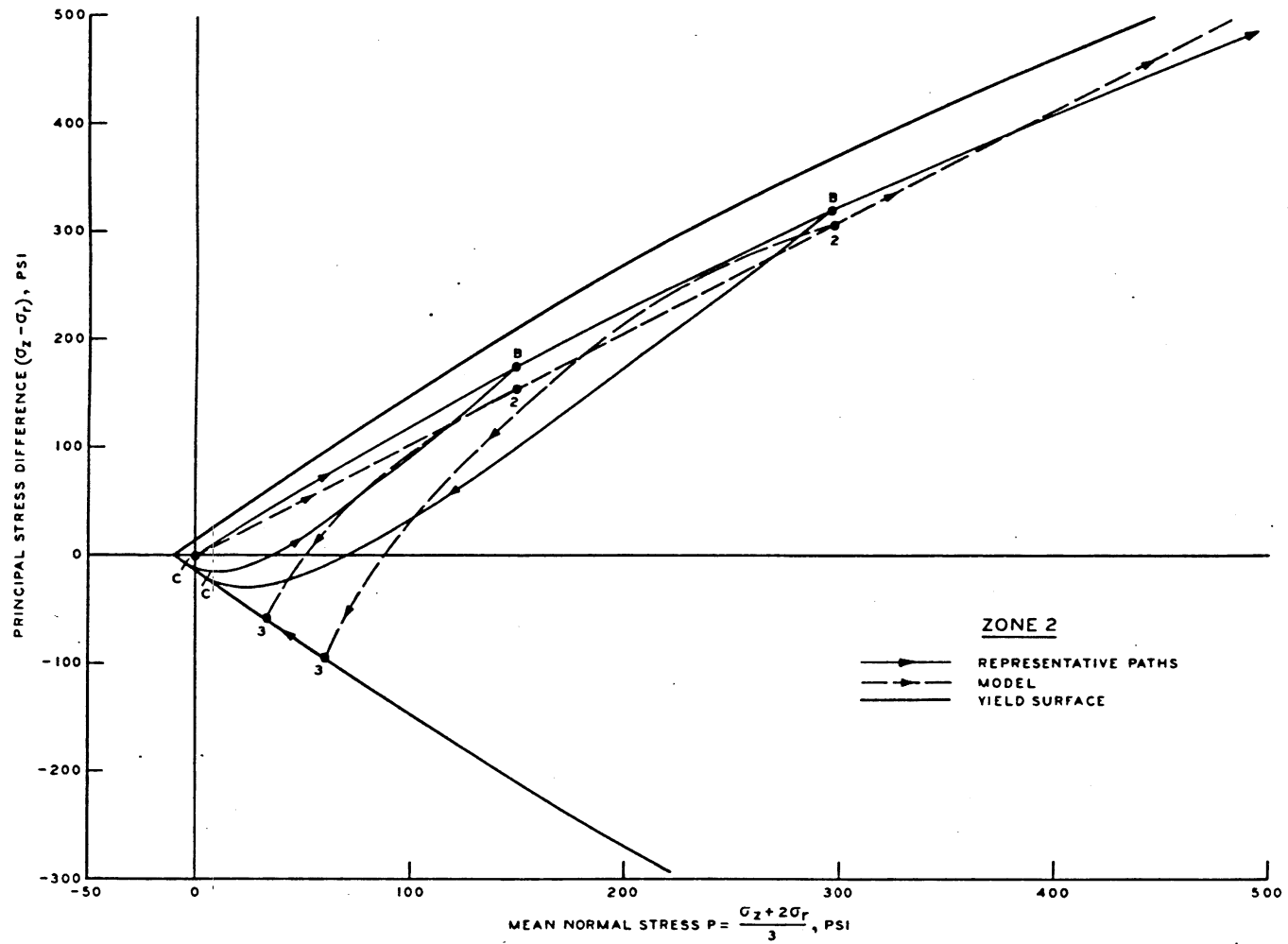


Figure 2.9 Comparison of representative dynamic stress paths in uniaxial strain with model fit; Zone 2, Prairie Flat.

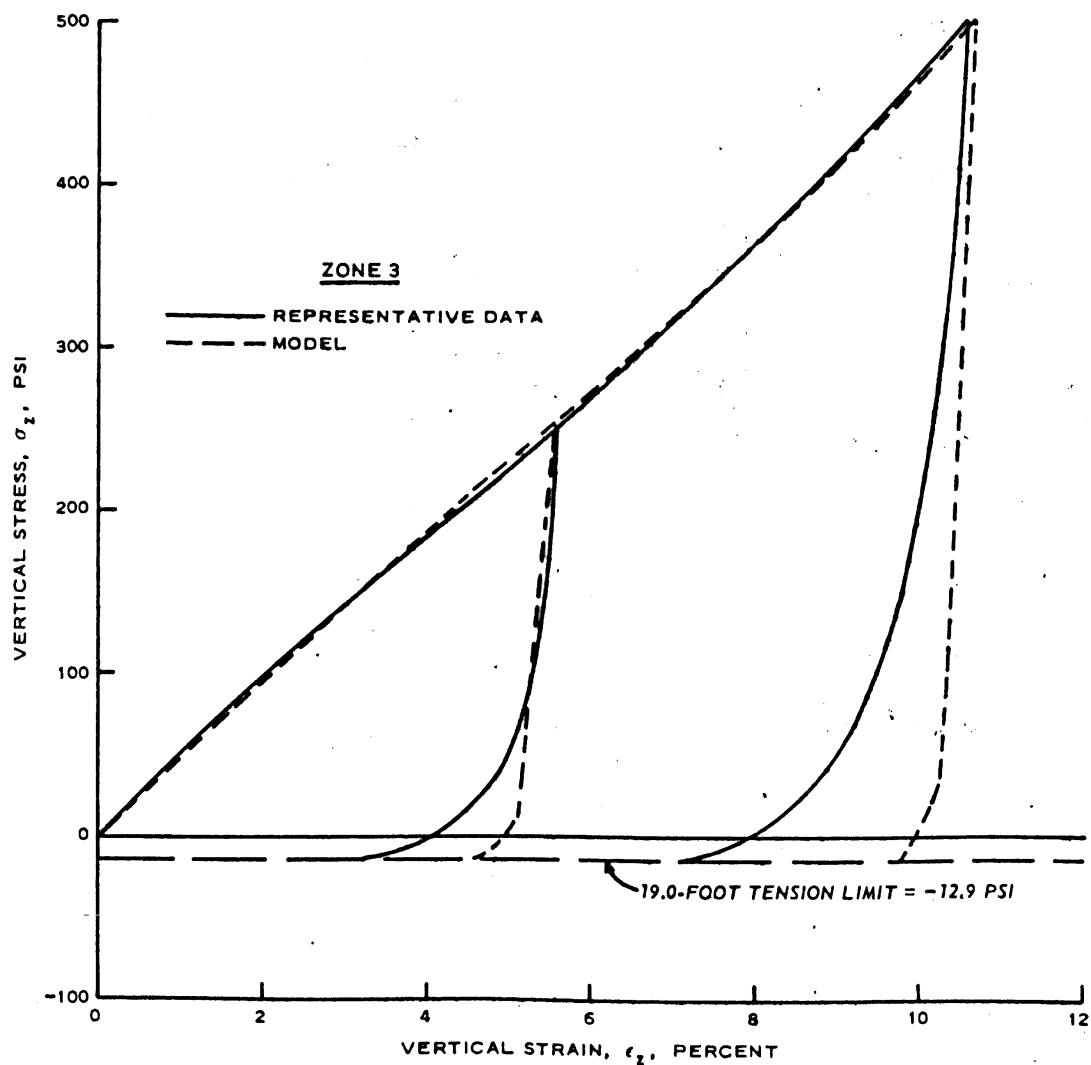


Figure 2.10 Comparison of representative dynamic uniaxial strain relations with model fit; Zone 3, Prairie Flat.

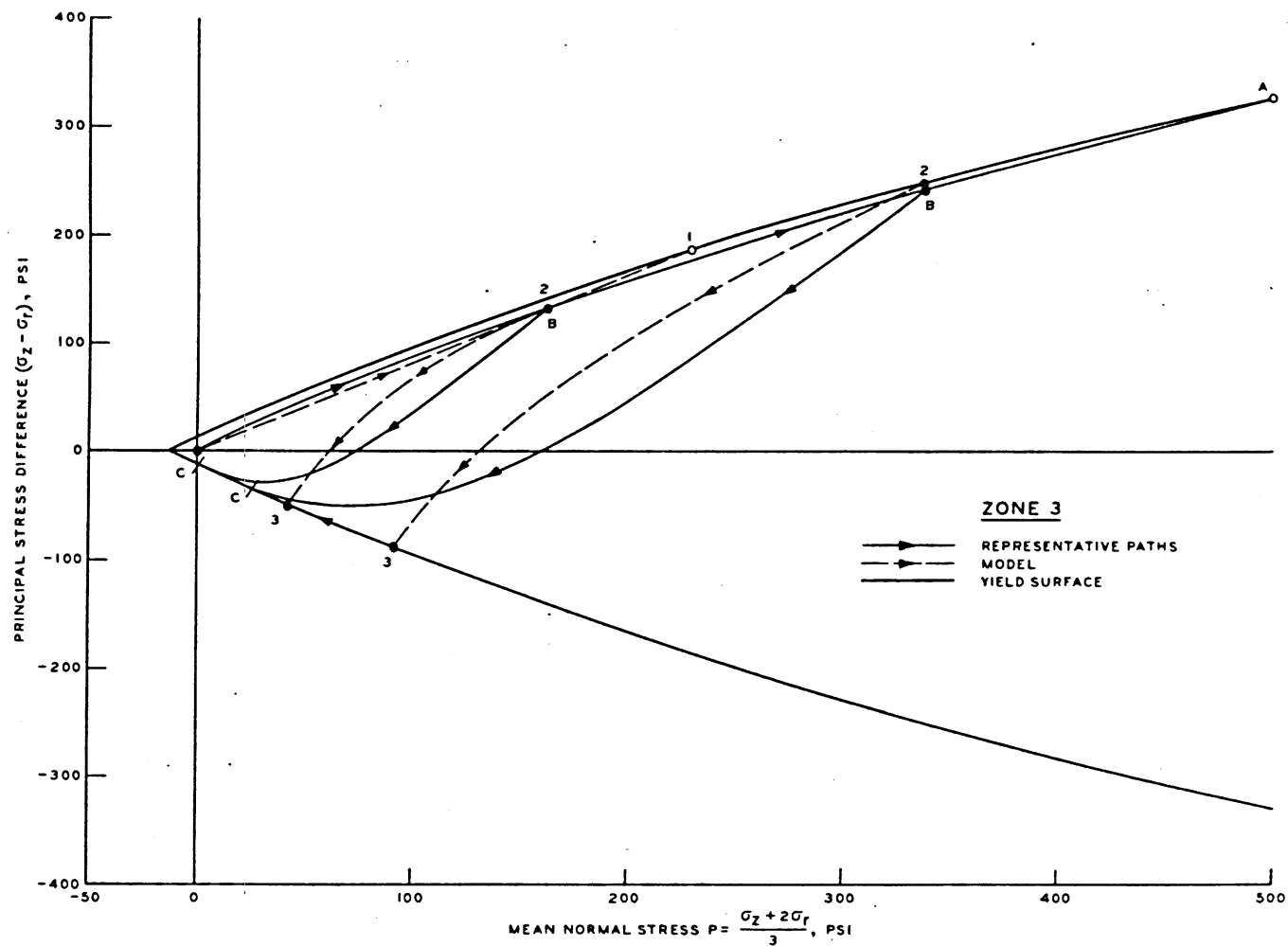


Figure 2.11 Comparison of representative dynamic stress paths in uniaxial strain with model fit; Zone 3, Prairie Flat.

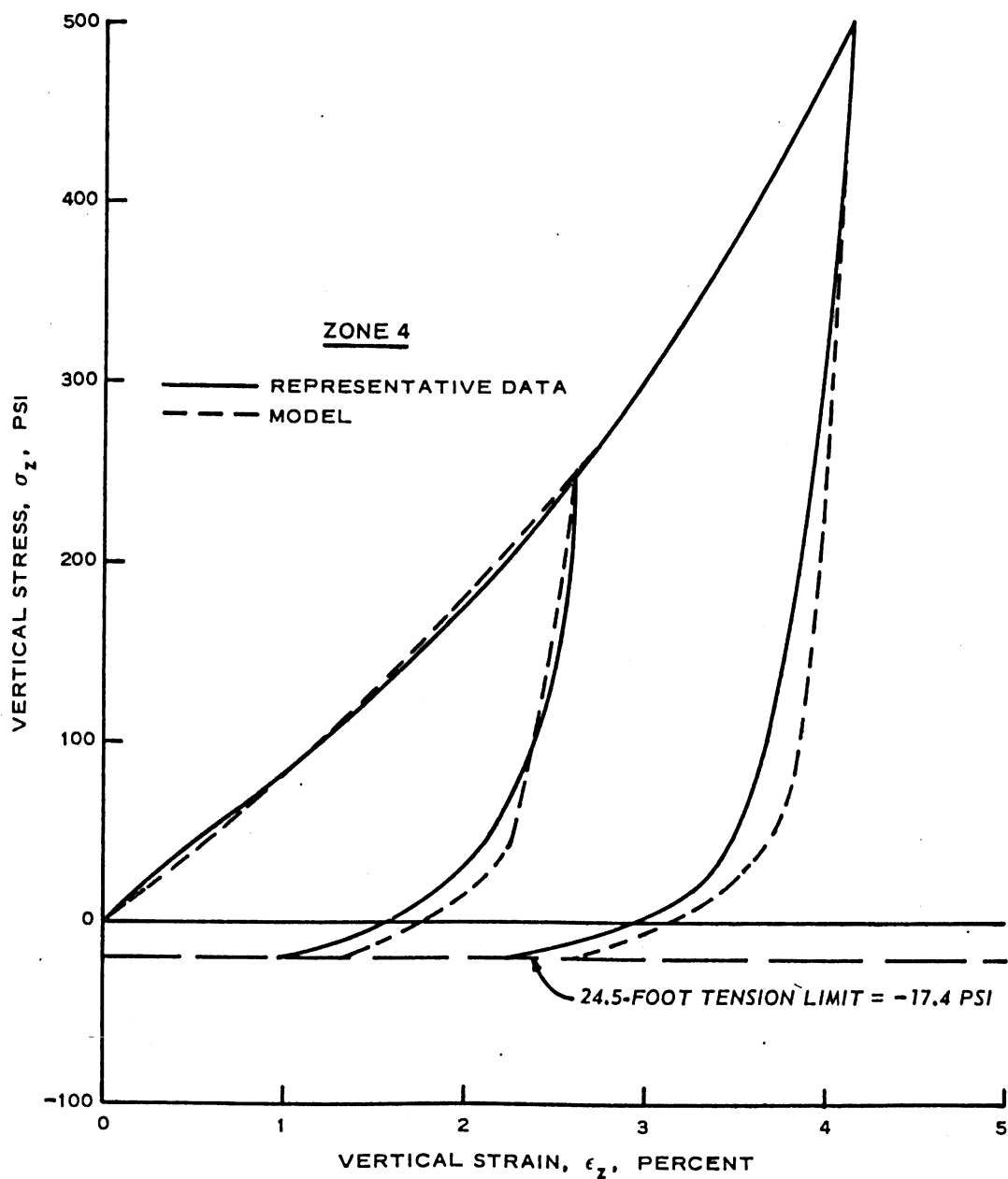


Figure 2.12 Comparison of representative dynamic uniaxial strain relations with model fit; Zone 4, Prairie Flat.

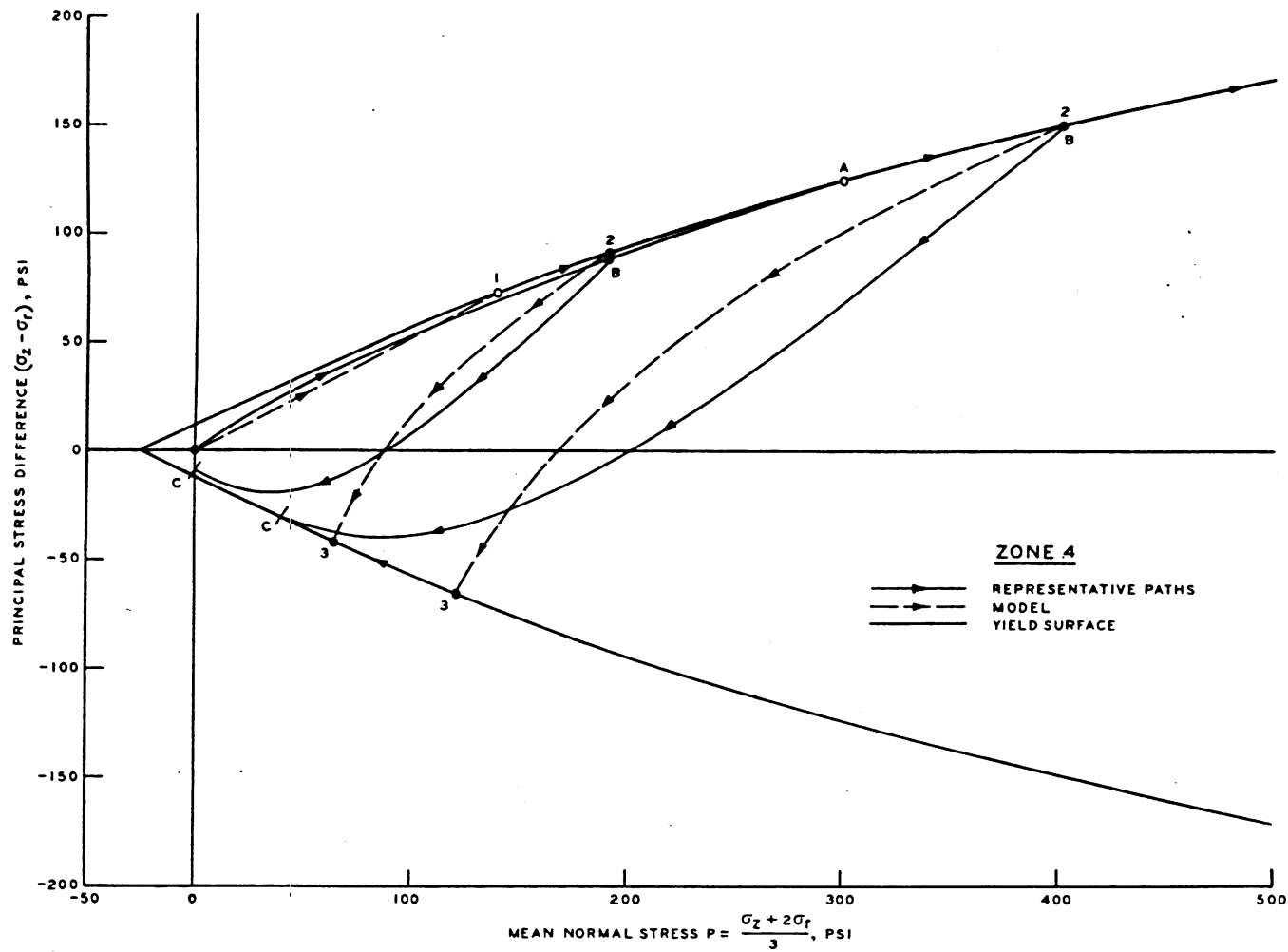


Figure 2.13 Comparison of representative dynamic stress paths in uniaxial strain with model fit; Zone 4, Prairie Flat.

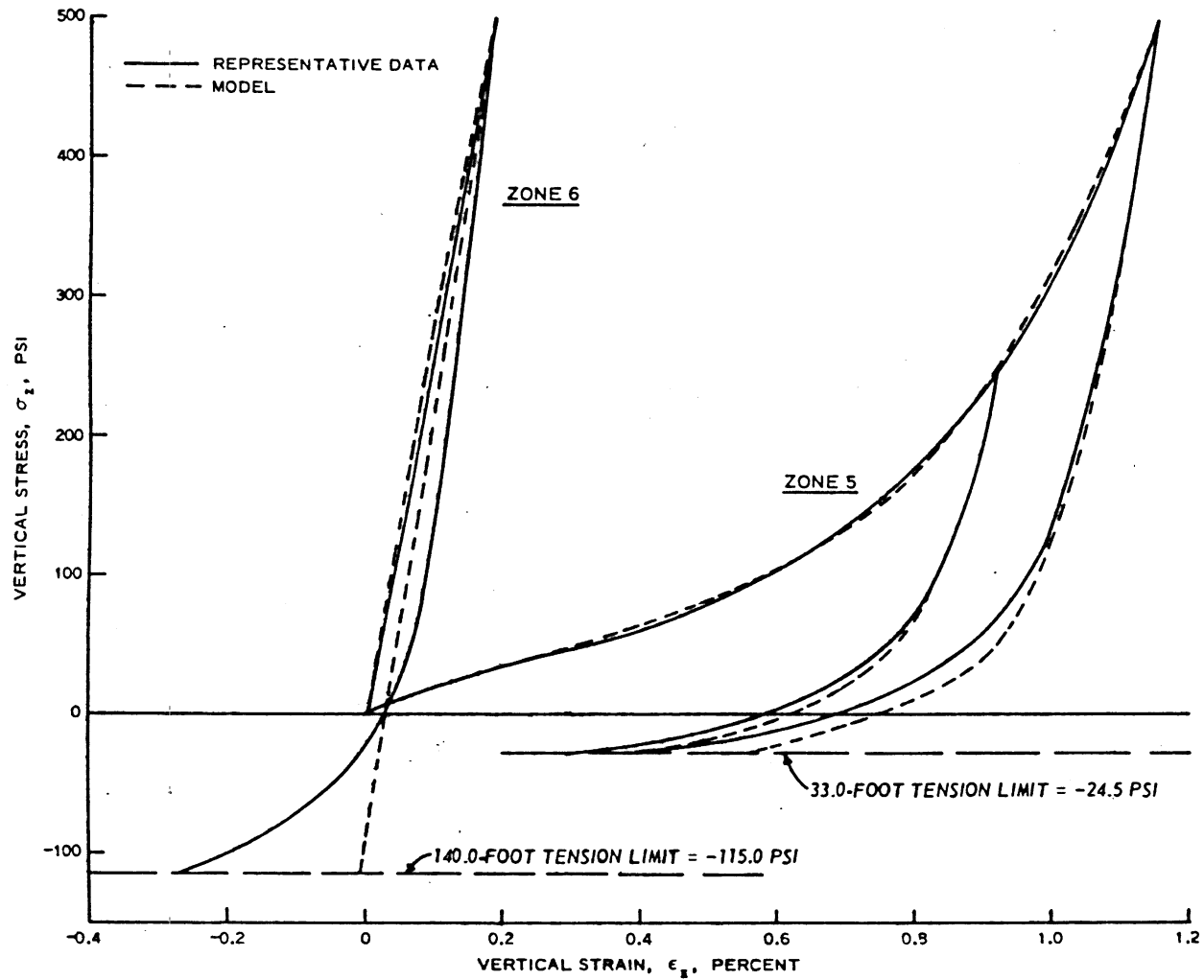


Figure 2.14 Comparison of representative dynamic uniaxial strain relations with model fit; Zones 5 and 6, Prairie Flat.

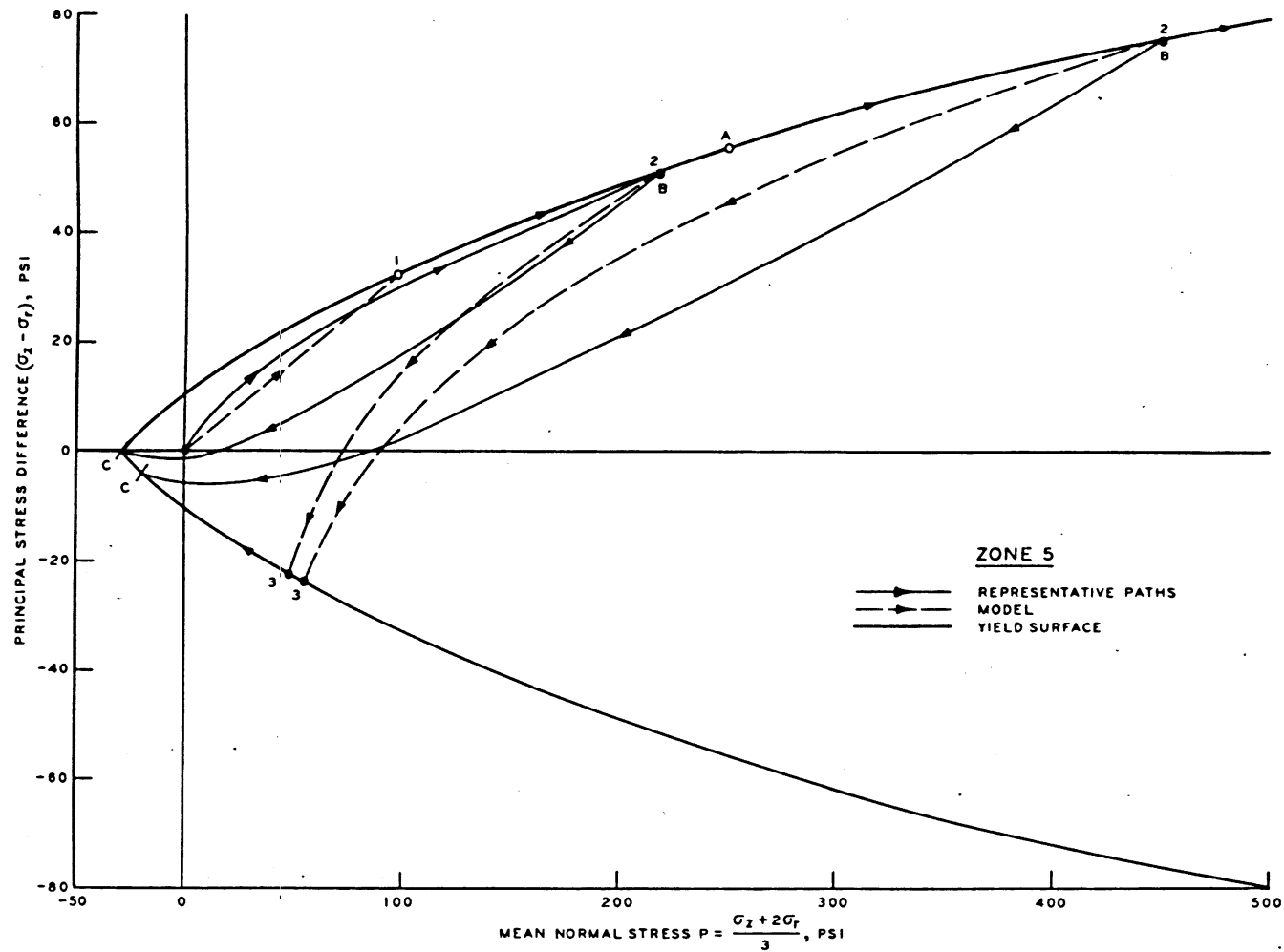


Figure 2.15 Comparison of representative dynamic stress paths in uniaxial strain with model fit; Zone 5, Prairie Flat.

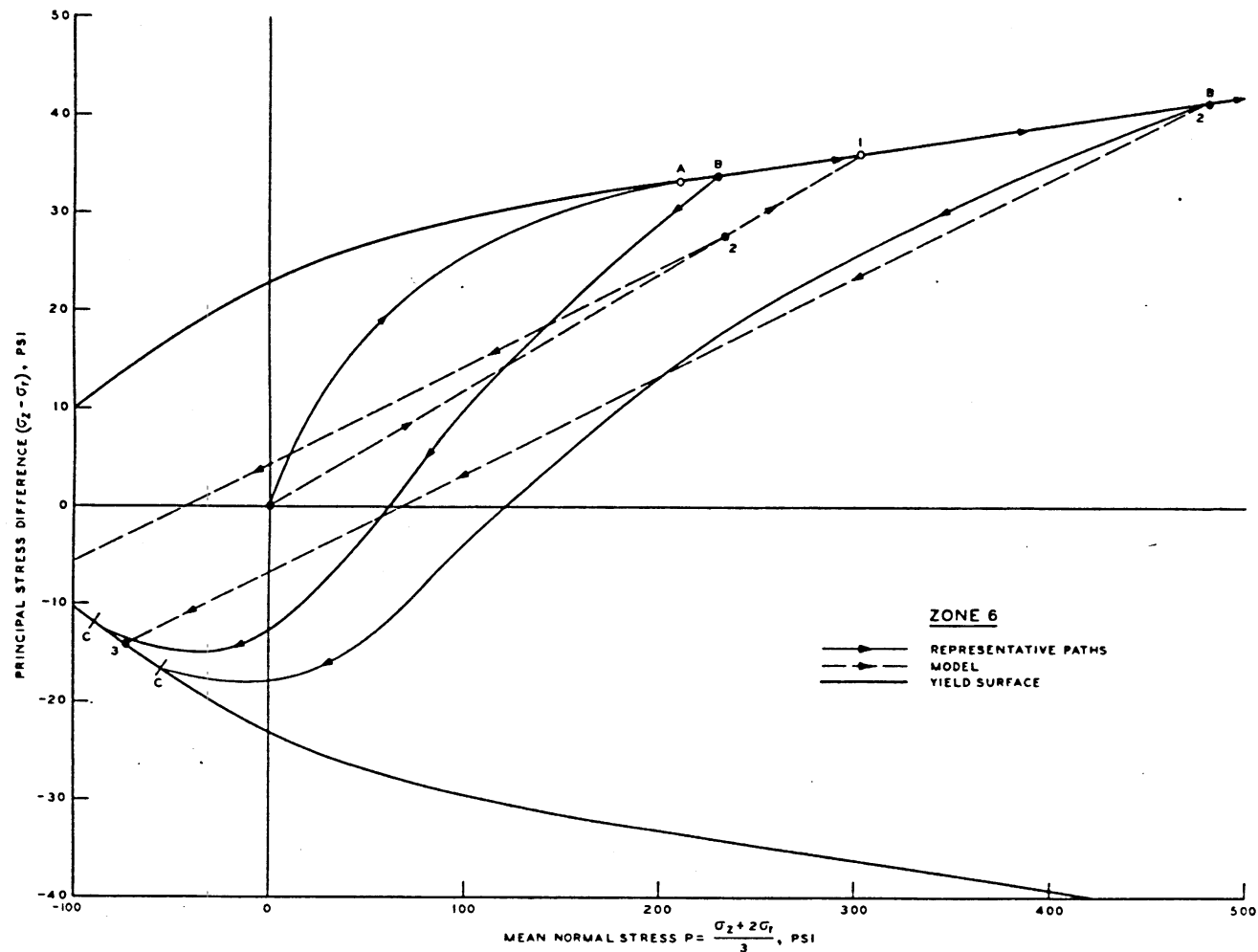


Figure 2.16 Comparison of representative dynamic stress paths in uniaxial strain with model fit; Zone 6, Prairie Flat.

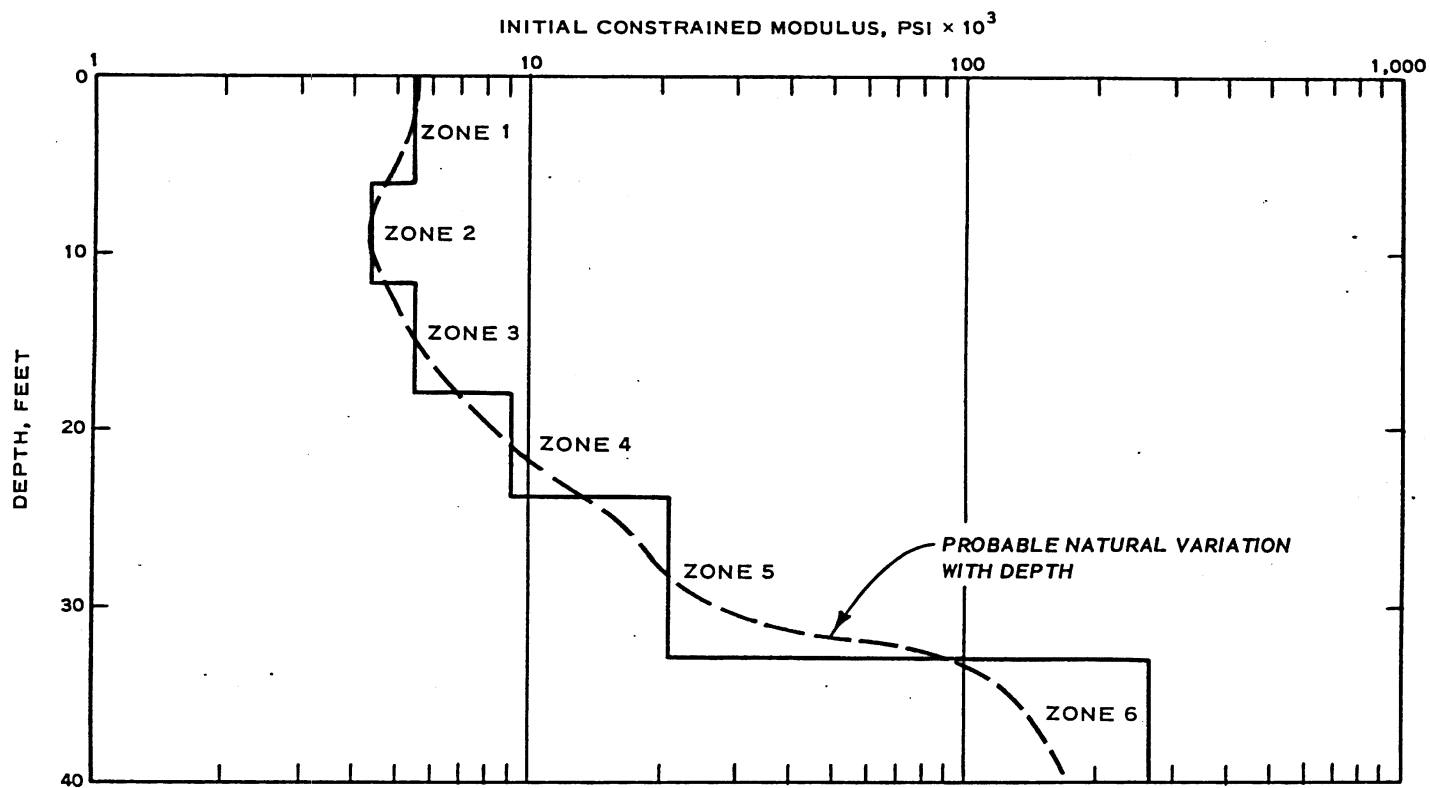


Figure 2.17 Variation of initial dynamic constrained modulus with depth; Prairie Flat.

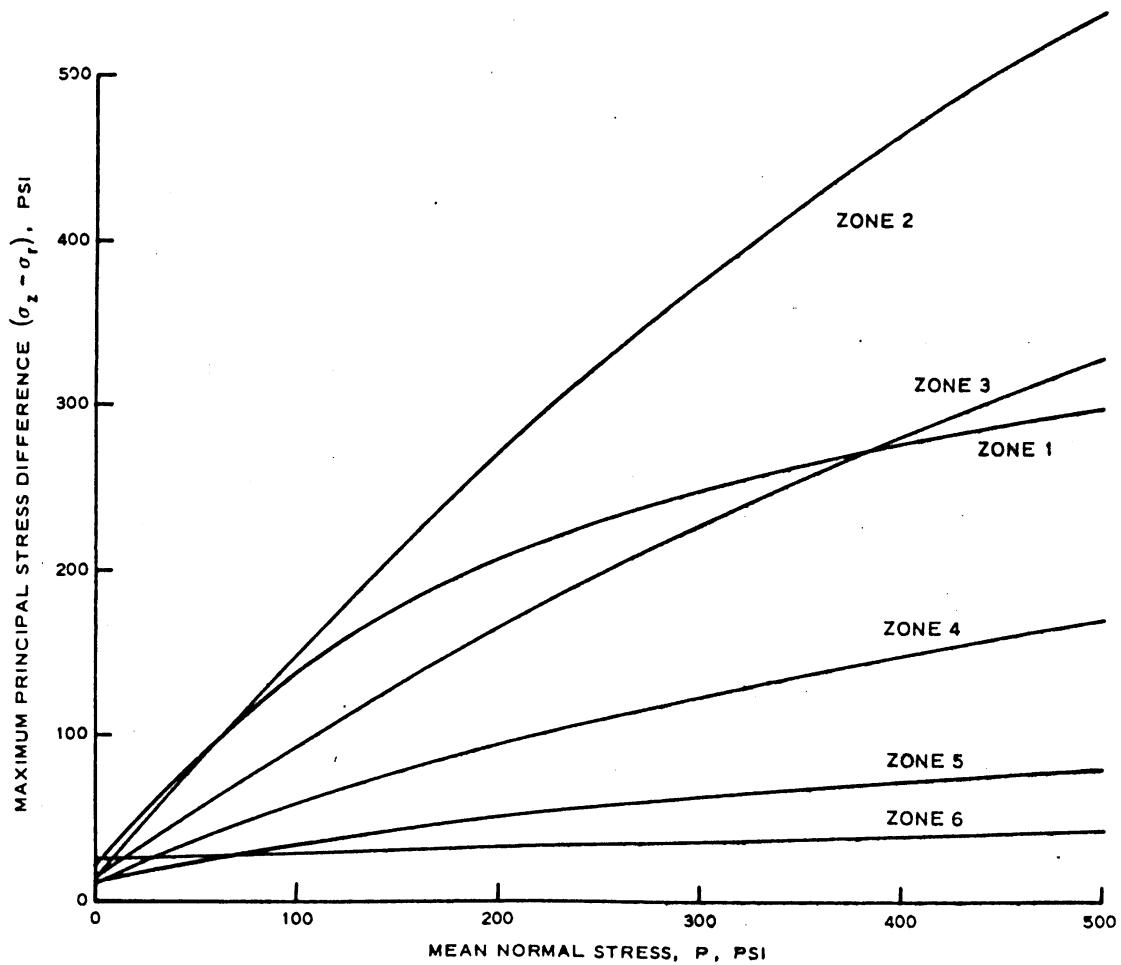


Figure 2.18 Comparison of representative dynamic shear strength properties, Zones 1 through 6, Prairie Flat.

CHAPTER 3

COMPUTATION DETAILS

3.1 CODED PROBLEM

The coded problem is shown schematically in Figure 3.1. The region considered for the calculation extended horizontally from ground zero (GZ) to a range of 555 feet and vertically to a depth of 75 feet. The bottom boundary was specified to be rigid-fixed, the far boundary was set free of radial gradients of stress, and the symmetry axis was, of course, free of shear stress and able to move vertically only. A mathematical air overpressure routine developed at WES was used to prescribe the time-dependent surface boundary condition; discussed in detail in the next section, this routine smoothly describes the actual Prairie Flat overpressure history between the nominal 1,500- and 40-psi contours (range = 84 and 560 feet, respectively). Between ground zero and 84 feet, an artificial pulse was applied to the surface.

A 3-foot square grid size and a time step of 0.5 msec were used to carry the 2D finite-difference calculation to a real time (from detonation) of 300 msec. The problem required approximately 3 hours of computer processor time.

3.2 AIR OVERPRESSURE FUNCTION

Airblast measurements obtained during the Prairie Flat event (Reference 5) were utilized to develop a mathematical expression for overpressure as an exponential interpolation function of range and time. In constructing the function, measured arrival times, peak pressures, and impulses were preserved as closely as possible.

The functional form of the derived fit (valid for ranges between 84 and 560 feet) is patterned after that used in the Weidlinger

calculation of Event Distant Plain 1A (Reference 2):

$$\begin{aligned} \sigma_{zz}(R,t) = & A(R) \times \left(B \exp \left\{ - A_1(R) \times [t - t_a(R) - t_r] \right\} \right. \\ & \left. + C \exp \left\{ - A_2(R) \times [t - t_a(R) - t_r] \right\} \right) \times \left[1 - \frac{t - t_a(R) - t_r}{t_d(R)} \right] \\ & \times U[t - t_a(R)] \times U[t_a(R) + t_d(R) + t_r - t] \end{aligned} \quad (12)$$

where:

σ_{zz} = surface pressure (tension considered positive), kips/in²

R = ground range, feet

t = time in milliseconds

U(x) = unit step functions

$A_1(R)$ and $A_2(R)$ = functions related by

$$A_1(R) = 10A_2(R) = \frac{14.0}{t_d(R)} \quad (13)$$

and B and C are constants:

$$B = 0.67$$

$$C = 0.33$$

The peak amplitude $A(R)$, the arrival time $t_a(R)$, and the positive duration $t_d(R)$ functions are determined from expressions of the form

$$f(R) = f_i + \frac{(f_{i+1} - f_i)}{(R_{i+1} - R_i)^\alpha} (R - R_i)^\alpha \quad R_i \leq R \leq R_{i+2} \quad (14)$$

where the exponent is given by

$$\alpha = \frac{\ln[(f_{i+1} - f_i)/(f_{i+2} - f_i)]}{\ln[(R_{i+1} - R_i)/(R_{i+2} - R_i)]} \quad (15)$$

Experimental values of arrival time, peak overpressure, and the adjusted positive durations used in the above equations are given in Table 3.1. A constant rise time $t_r = 0.25$ msec was appended to the overpressure function to provide agreement with the field airblast measurements.

In the region $0 \leq R < 84$ feet, the artificial overpressure applied to the surface was $\sigma_{zz}(84, t)$ with

$$t_a(R) = t_a(84) \times \frac{R}{84} \quad (16)$$

The quality of the airblast fit is depicted in Figure 3.2, where it is compared with field measurements at ground ranges of 84, 220, 330, and 560 feet.

TABLE 3.1 SURFACE OVERPRESSURE FUNCTION PARAMETERS

| Ground Range R | Arrival Time $t_a(R)$ | Peak Overpressure $-A(R)$ | Positive Duration $t_d(R)$ |
|-------------------|--------------------------|------------------------------|-------------------------------|
| feet | msec | kips/sq in | msec |
| 84 | 5.3 | 1.5174 | 11.1 |
| 140 | 11.0 | 0.8103 | 13.9 |
| 220 | 22.2 | 0.495 | 25.0 |
| 240 | 25.4 | 0.3966 | 45.0 |
| 400 | 63.5 | 0.1063 | 110.0 |
| 475 | 89.7 | 0.0744 | 135.0 |
| 560 | 125.5 | 0.0378 | 250.0 |

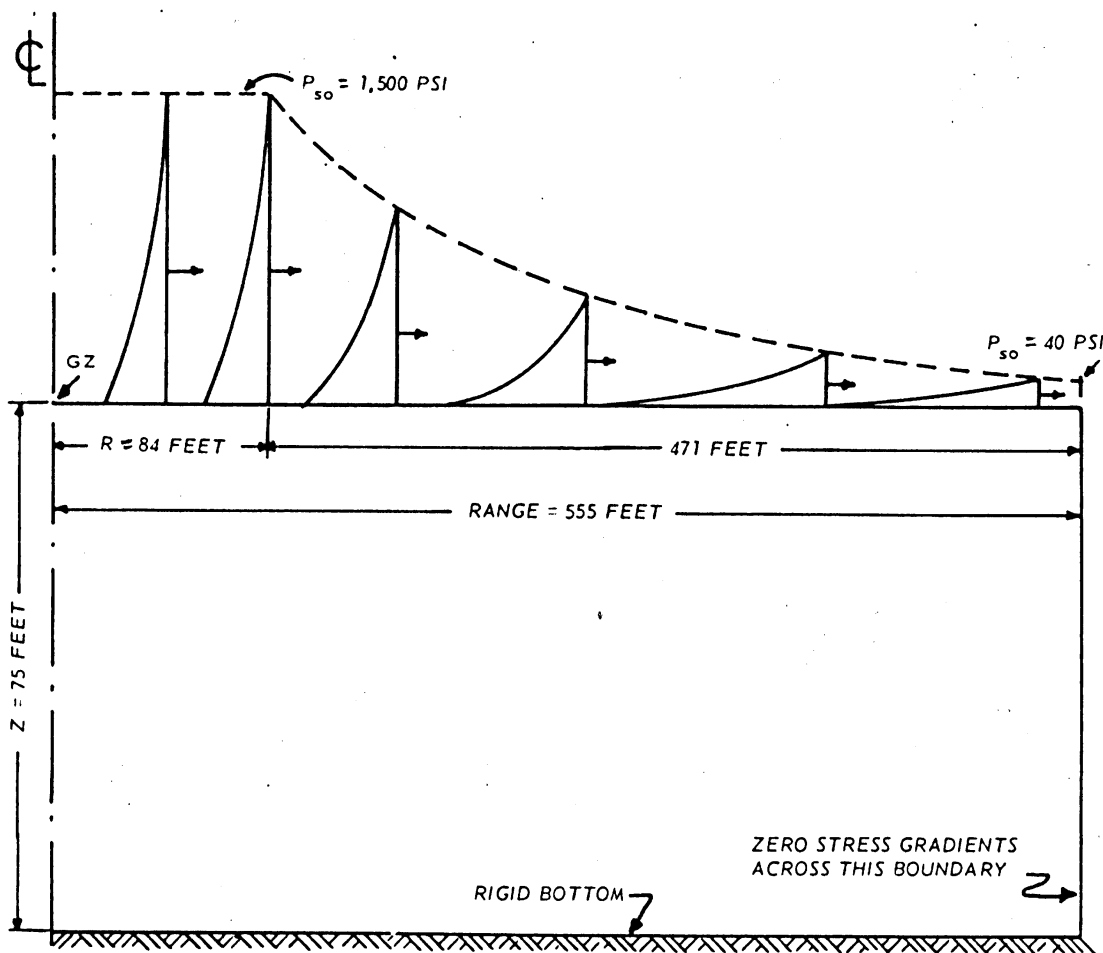


Figure 3.1 Schematic representation of coded Prairie Flat boundary value problem.

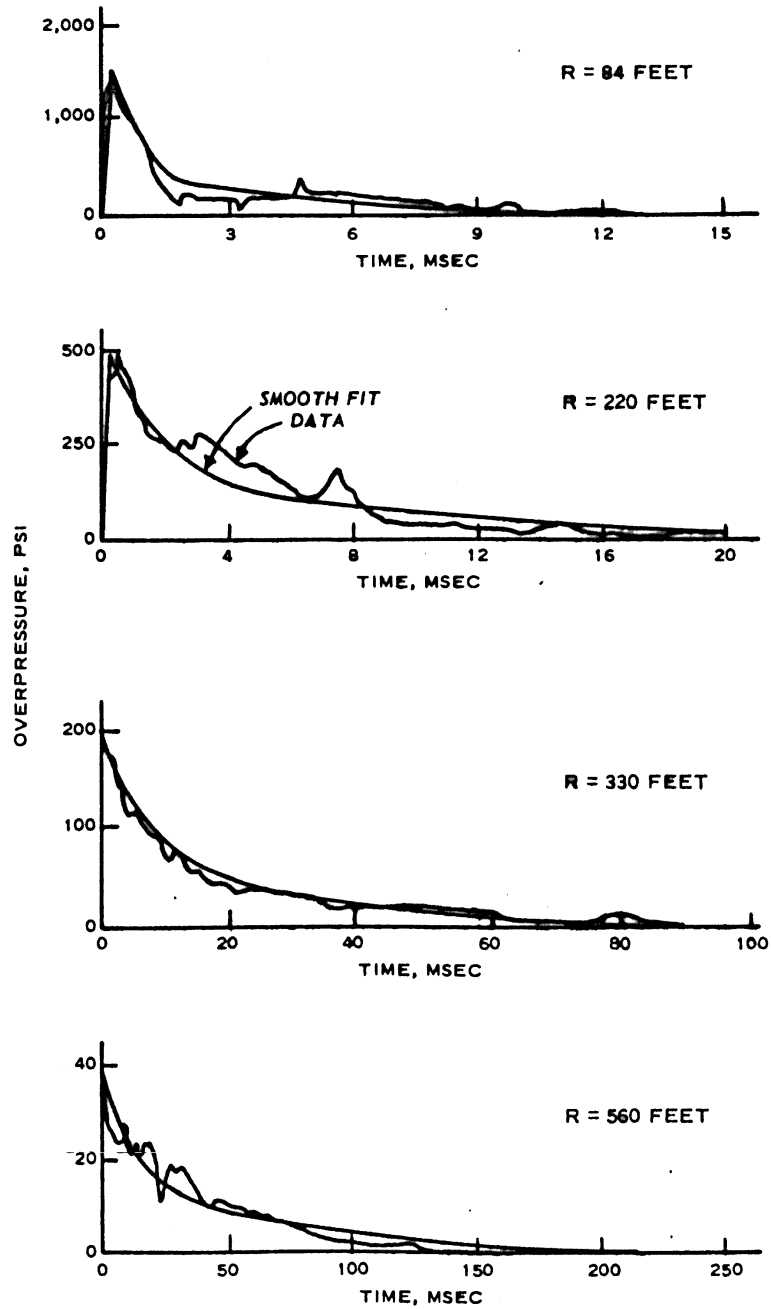


Figure 3.2 Comparison of mathematical fit with Prairie Flat air overpressure measurements at selected ground ranges.

CHAPTER 4

RESULTS

4.1 GENERAL

The field data utilized in this report were obtained from the Project Officer in charge of the WES ground-motion measurement experiment for Operation Prairie Flat. A description of the WES experiment and portions of the measured data have been published (Reference 6). The measurements are considered reliable; however, they are still subject to future modification.

The results of the 2D calculation are compared with the field measurements at two intermediate ground ranges, $R = 220$ feet (nominal 500-psi contour) and $R = 330$ feet (nominal 200-psi contour), where code output was least prone to artificial boundary influences. Computed waveforms at depths of 1.5, 4.5, 10.5, and 16.5 feet are compared with corresponding field data obtained at depths of 1.5, 5.0, 10.0, and 17.0 feet.

4.2 PRELIMINARY CODE STUDIES

Prior to the 2D calculation, a series of one-dimensional (1D) runs were made, using the nominal 800-psi contour overpressure pulse, to parametrically study the effect of grid size and time step. This study showed that time-step variations satisfying the Courant criterion (Reference 7) would have negligible effect on the computed vertical waveforms. However, it also showed that grid-size variations would significantly influence computed peak stresses and particle velocities in the immediate vicinity of the surface.

The results of the grid-size study are summarized in Figure 4.1 where the attenuations of computed peak vertical particle velocity are compared for grid dimensions of 0.75, 1.5, and 3.0 feet; field data

obtained at this range (140 feet) and the results of the 2D calculation are included in the figure for completeness sake. As grid size increased, more and more of the high-frequency spike of the airblast front was lost in the 1D calculations; however, little impulse was lost as a result, and below a depth of about 5 feet, the calculated peaks converged (as did the remainder of the waveforms). This study indicated that a very fine grid is needed in the vicinity of the surface to minimize ground shock underprediction for HE tests conducted at the Watching Hill site.

The 2D calculation suffered an even greater loss of the high-frequency airblast spike due to horizontal as well as vertical grid-size effects. The surface node at this range did not experience its mathematically predicted peak overpressure (810 psi, Table 3.1) during the incremental sweep of the airblast function; it only saw a peak of 732 psi. This accounts for a portion of the 1D-2D discrepancy in Figure 4.1. This problem can be alleviated somewhat (if running time is not a problem) by reducing the time step.

Another series of one-dimensional runs were made using the overpressure pulses pertinent to the 800- and 200-psi contours in order to assess the influence of the rigid bottom boundary location on code output in this region. Rigid boundaries at depths of 75, 150, and 250 feet were considered (bedrock at the site is located in the vicinity of 250 feet). The results showed detectable quantitative, but not qualitative, differences in the vertical motions at later times. The differences were sufficiently minor to suggest running the first 2D calculation of the Prairie Flat constitutive model parameter study with the 75-foot-deep boundary. The influences of the bottom boundary location on the late-time computed horizontal motions will be assessed in future 2D calculations.

4.3 VERTICAL MOTIONS

Figures 4.2 and 4.3 show comparisons of the experimental and computed vertical particle-velocity waveforms at the 220- and 330-foot ranges, respectively. The correlations are quite favorable at all locations. The oscillations in the computed waveforms are partially due to the numerical techniques employed in the code and partially due to real stress-wave interactions in the multilayered profile; separation of these effects also awaits additional calculations.

As suggested by the grid-size effects study, the computed peaks at the 1.5-foot depth at both ranges are lower than the measured peaks by about a factor of two. The discrepancy in the peaks at depth 17 feet, range 330 feet, is partially attributable to the fact that the gage recorded an early-arriving outrunning signal well prior to the arrival of the local airblast energy.

Comparisons of the computed and measured vertical displacement waveforms at the 220- and 330-foot ranges are shown in Figures 4.4 and 4.5, respectively. The measurements represent integrated particle-velocity gage records. The agreements are generally good although the phasing of the computed waveforms appears to lag that of the measurements. The late-time measurement at depth 1.5 feet, range 220 feet, is suspect.

Ground shock attenuation with depth at the 220- and 330-foot ranges is summarized in Figures 4.6 and 4.7, respectively, where computed peak vertical particle velocities and displacements are compared with the measured peaks. The dashed portions of the computed curves are a reminder that the calculated peaks are questionable in the vicinity of the surface (see Figure 4.1).

The combined effects of the short duration of the Prairie Flat airblast pulse and the highly compressible and energy-absorbing nature of the materials in the upper zones of the profile resulted in an

initially extremely rapid attenuation of incident peak vertical velocity and stress with depth. As the groundwater table was approached, further reductions in incident peak velocity occurred while peak stresses were simultaneously enhanced due to reflection-refraction phenomena at the higher impedance interfaces. Figure 4.8 shows the computed attenuation of peak dynamic vertical, radial, and mean normal stresses versus depth for the 220- and 330-foot ranges.

The calculation revealed that the major upward-traveling reflected stress pulse generated when the incident wave impinged on the stiff materials in the vicinity of the groundwater table was a significant factor in arresting or reversing the downward momentum of the materials above the water table. In its subsequent refraction from the surface (which by then was free of positive overpressure), this pulse became a tensile rarefaction that imparted new or additional upward momentum to the near-surface soils, spalling or fracturing them as it passed (i.e., the tension cutoff, Chapter 2, was invoked). The spalled materials essentially behaved as groups of free particles acted upon only by gravity with each particle having an initial velocity vector. Eventually, after following ballistic trajectories, the particles came back into contact with one another to reconstitute the continuum. This phenomenon can be readily observed in the velocity waveforms shown in Figures 4.2 and 4.3. Near-surface spalling occurred in the time period 100 to 125 msec at range 220 feet and in the period 125 to 150 msec at range 330 feet. Both the calculation and the measurements indicate that the vertical velocities decrease at an approximately linear rate ($\approx 32.2 \text{ ft/sec}^2$) for periods ranging from 100 to 200 msec after spall inception. This free-fall effect was computed at all code output ranges.

4.4 RADIAL MOTIONS

Calculated radial velocity waveforms are compared with the field measurements at ground ranges of 220 and 330 feet in Figures 4.9 and 4.10, respectively. The peak radial velocities are smaller than the vertical peaks by approximately one order of magnitude; this indicates that a highly superseismic condition existed at these depths and ground ranges. The computed motions at early times generally agree in form and magnitude with the measurements. For example, first-arrival outward velocity peaks show little or no attenuation with depth and the consistently computed shear-wave-induced reversals immediately behind the first peaks have detectable counterparts in the data; however, as discussed in the previous section, the computed near-surface peaks are probably low because of grid-size effects. The individual oscillations beyond the first full cycle are partially due to realistic reflection-refraction phenomena and partially due to unrealistic numerical noise. Late-time correlations at range 220 feet could be improved by considering the higher energy inputs closer to ground zero. Further calculations are required to clarify these details.

The computed radial velocities at depth 1.5 feet at both ground ranges are constant at later times as a result of the near-surface spall; these are the horizontal components of the ballistic trajectories discussed previously.

The 10- and 17-foot-deep gages at range 330 feet, Figure 4.10, indicated that low-amplitude outrunning signals were the first arrivals at these locations; this correlates with the vertical record for the 17-foot station, Figure 4.3.

The radial displacement waveforms are compared in Figures 4.11 and 4.12 for the 220- and 330-foot ranges, respectively. The late-time computations are, of course, partially suspect since the degree of influence of the bottom artificial boundary has yet to be

established, but the calculation mirrors the continuous outward flow of material recorded by the field gages.

The overpressure impulse at the 200 psi contour was greater than that at the 500 psi contour by approximately 30 percent (Reference 5); in addition, the duration was much longer. Thus, peak stress attenuation was less severe at the further ground range. This resulted in higher peak stresses in Zones 5 and 6 at $R = 330$ feet (see Figure 4.8), which in turn resulted in more plastic flow occurring in Zone 5 at this range than at $R = 220$ feet. This effect, in combination with the extra impulse, resulted in larger computed radial displacement peaks at $R = 330$ feet than at $R = 220$ feet (larger by at least a factor of two).

The measured peak radial displacements shown at $t = 300$ msec in Figures 4.11 and 4.12 represent 50 percent or more of the total outward displacements recorded at these locations in the Prairie Flat event due to the direct and airblast-induced energy inputs. The results of this calculation indicate that a significant portion of the near-surface radial displacement maxima is attributable to airblast effects alone. Finally, it is worth noting that the measured maximum radial displacements at these locations are the same general order of magnitude as the measured vertical maxima.

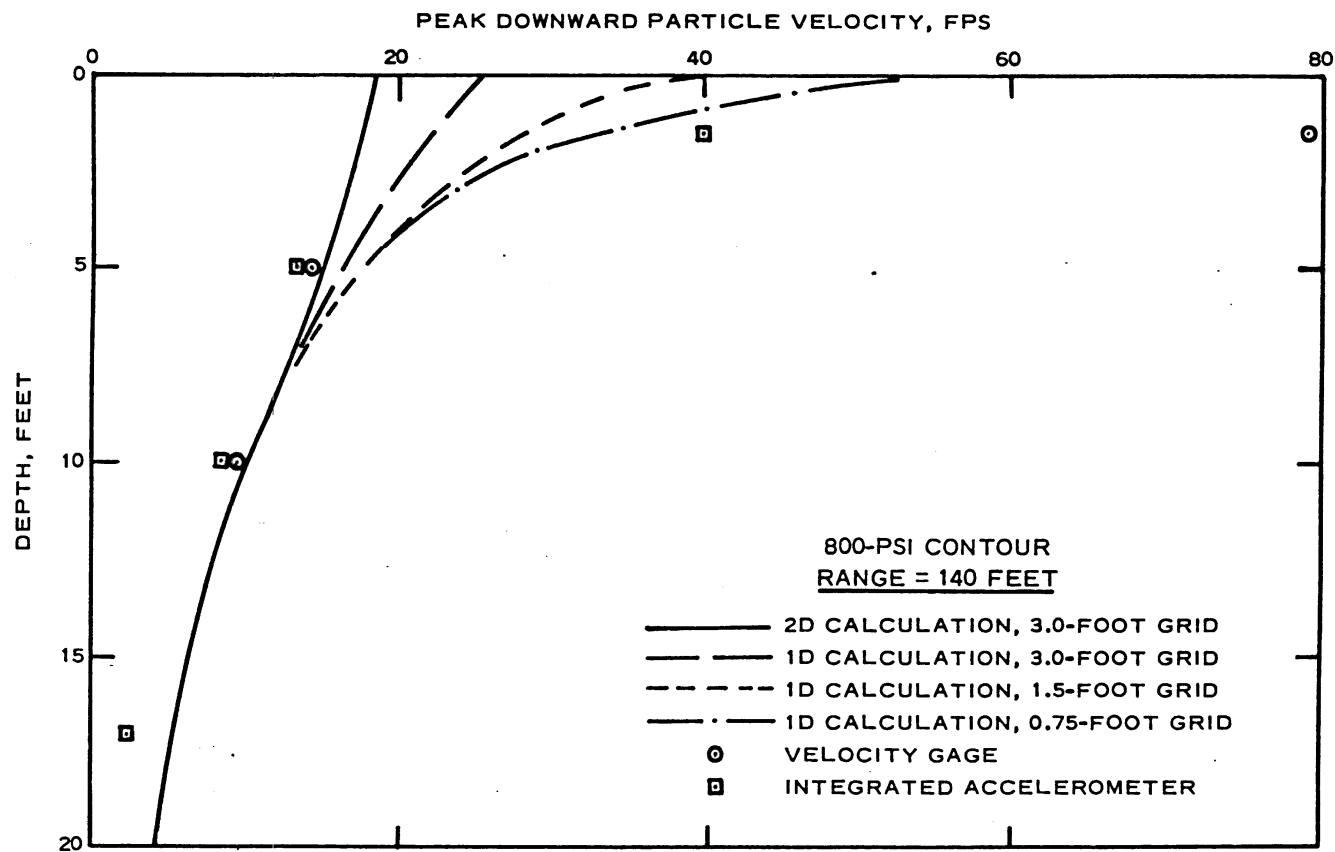


Figure 4.1 Results of grid-size parameter study at 800-psi contour.

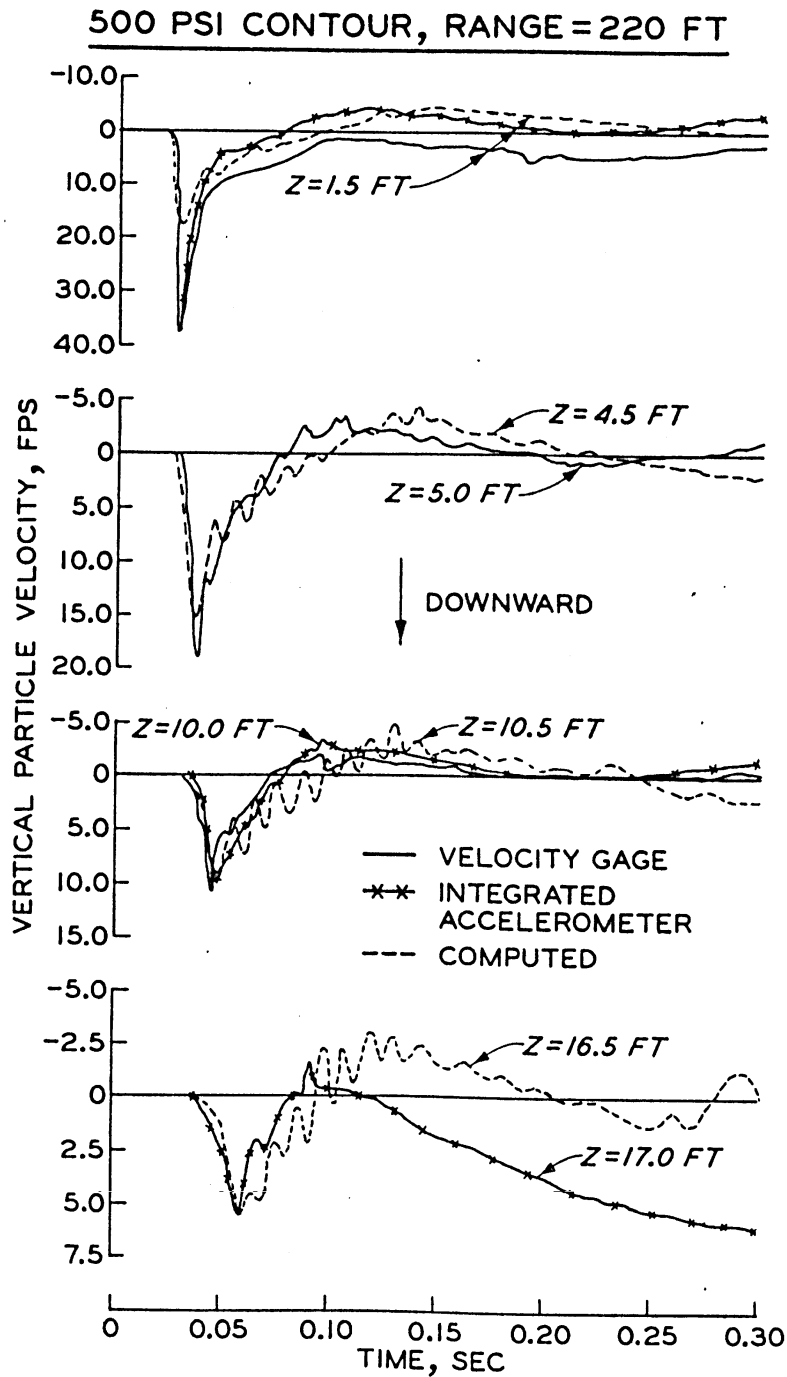


Figure 4.2 Comparison of computed vertical particle velocity waveforms with field measurements; range 220 feet; Prairie Flat.

200 PSI CONTOUR, RANGE= 330 FT

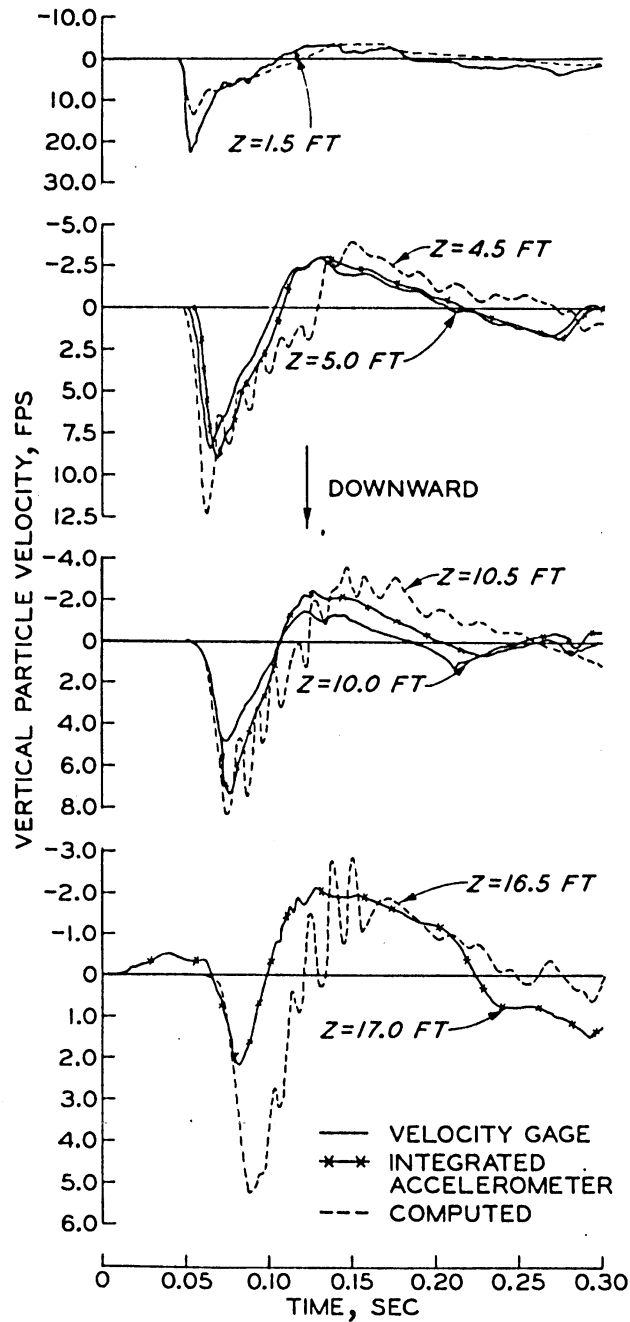


Figure 4.3 Comparison of computed vertical particle velocity waveforms with field measurements; range 330 feet; Prairie Flat.

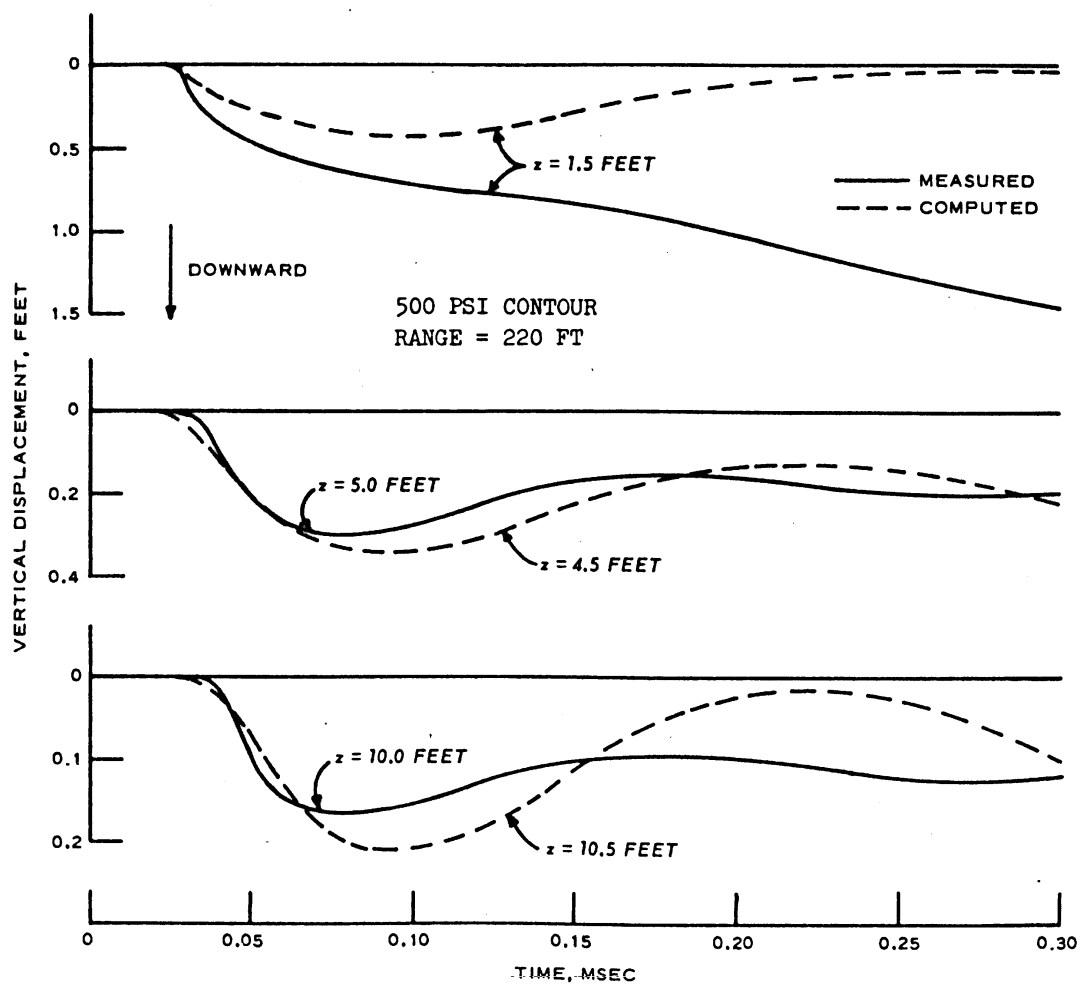


Figure 4.4 Comparison of computed vertical displacement waveforms with field measurements; range 220 feet; Prairie Flat.

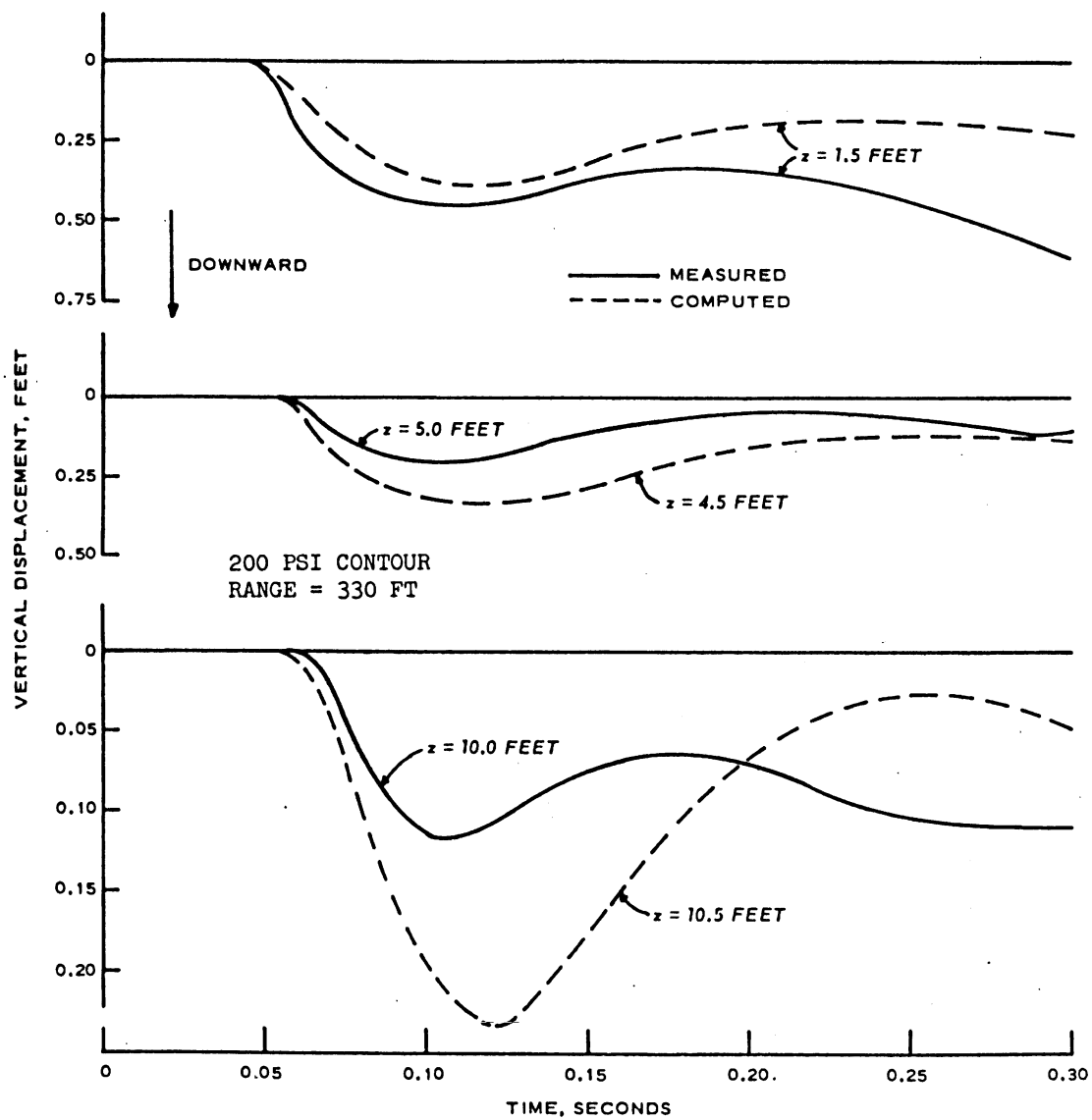


Figure 4.5 Comparison of computed vertical displacement waveforms with field measurements; range 330 feet; Prairie Flat.

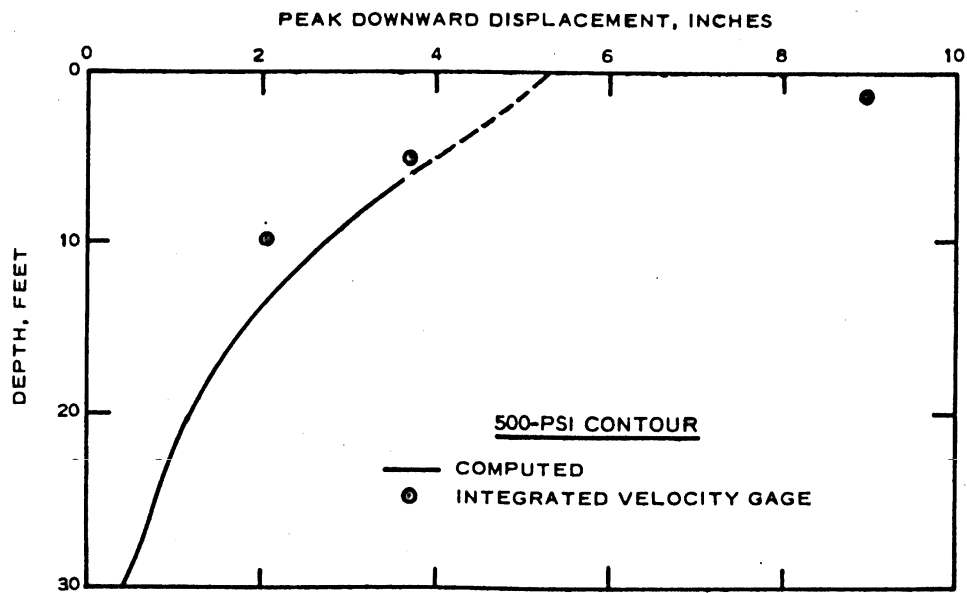
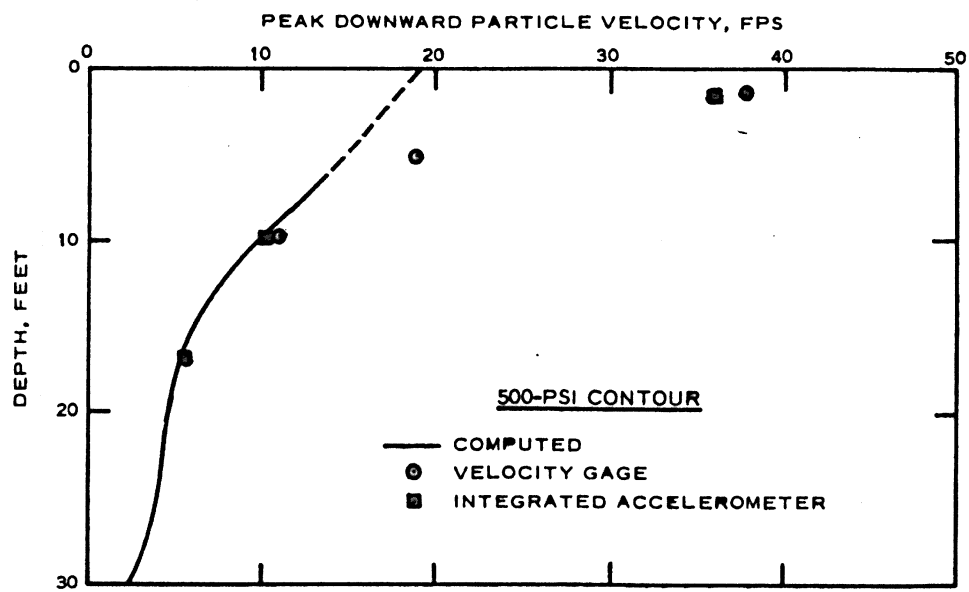


Figure 4.6 Comparison of measured and computed peak vertical particle velocity and displacement attenuations versus depth; range 220 feet; Prairie Flat.

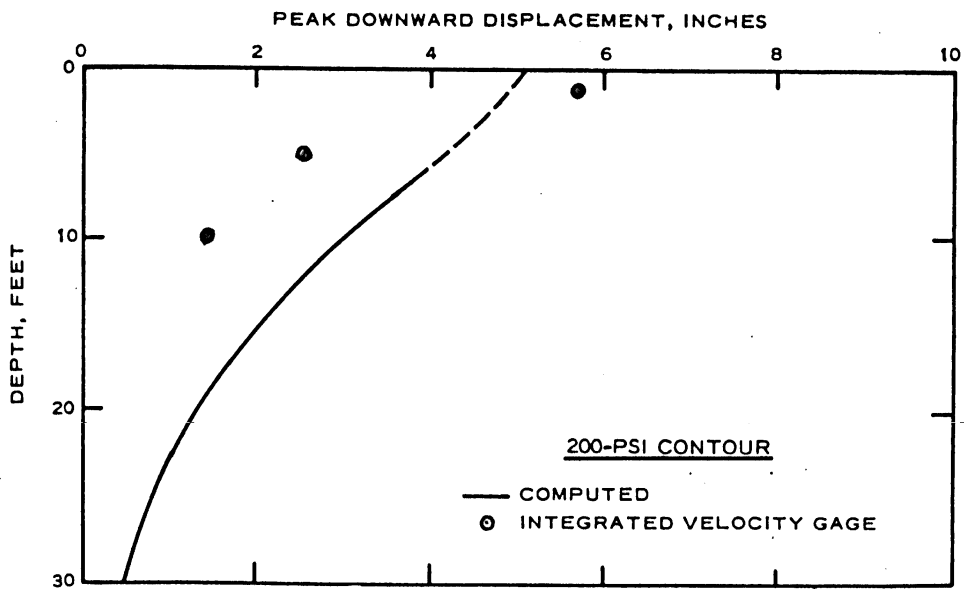
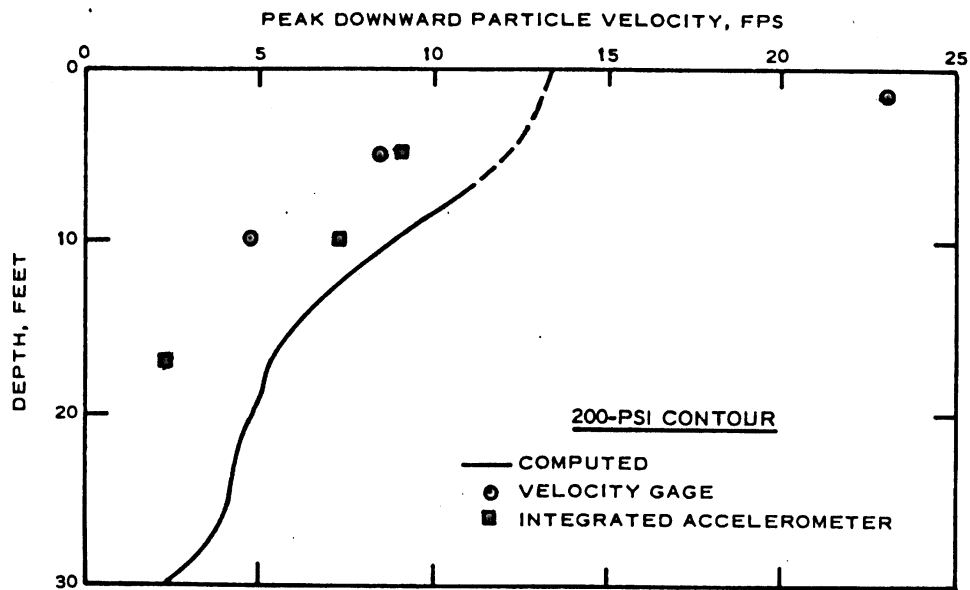


Figure 4.7 Comparison of measured and computed peak vertical particle velocity and displacement attenuations versus depth; range 330 feet; Prairie Flat.

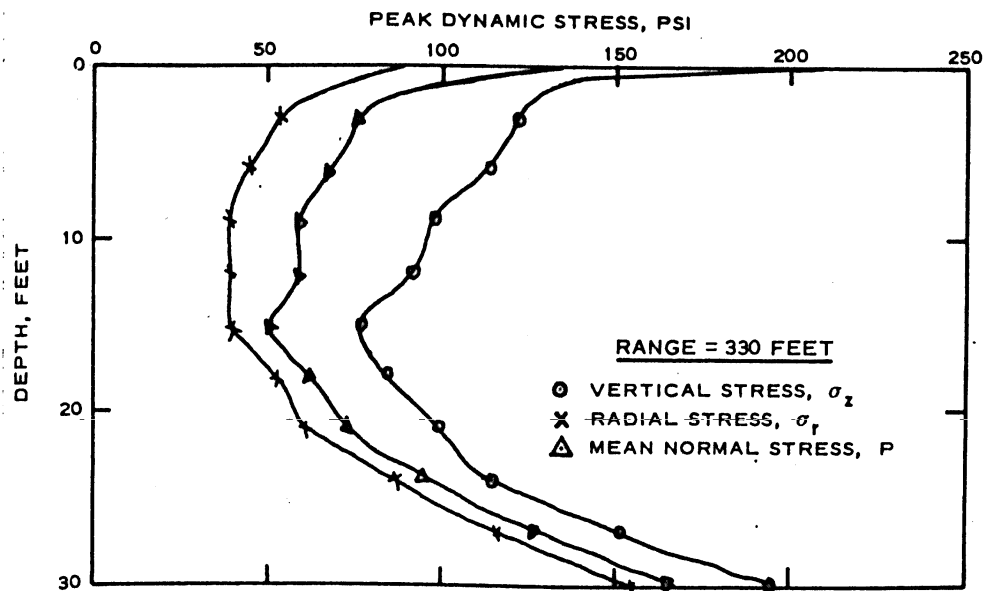
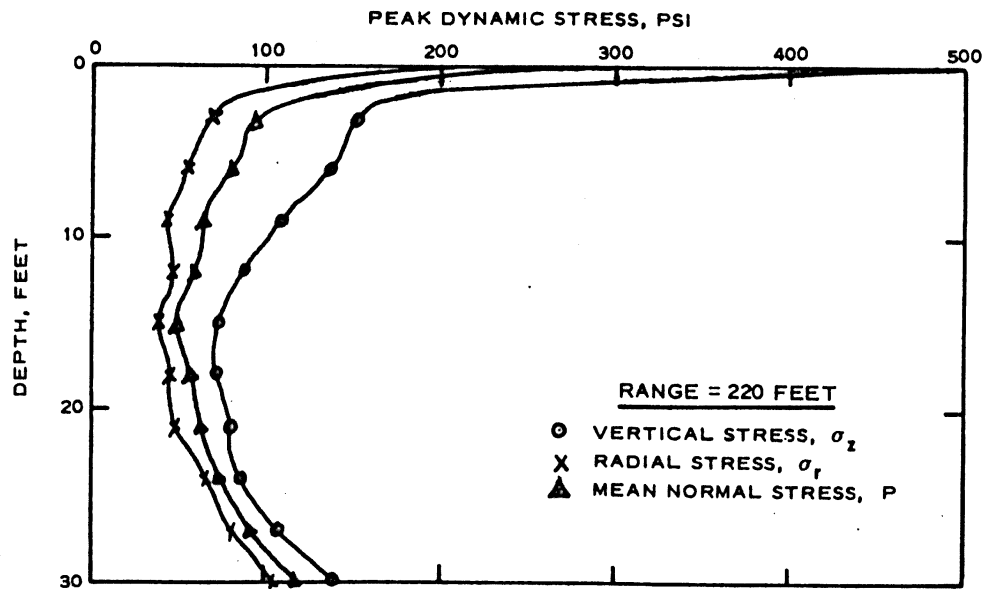


Figure 4.8 Computed attenuations of peak stress; ranges 220 and 330 feet; Prairie Flat.

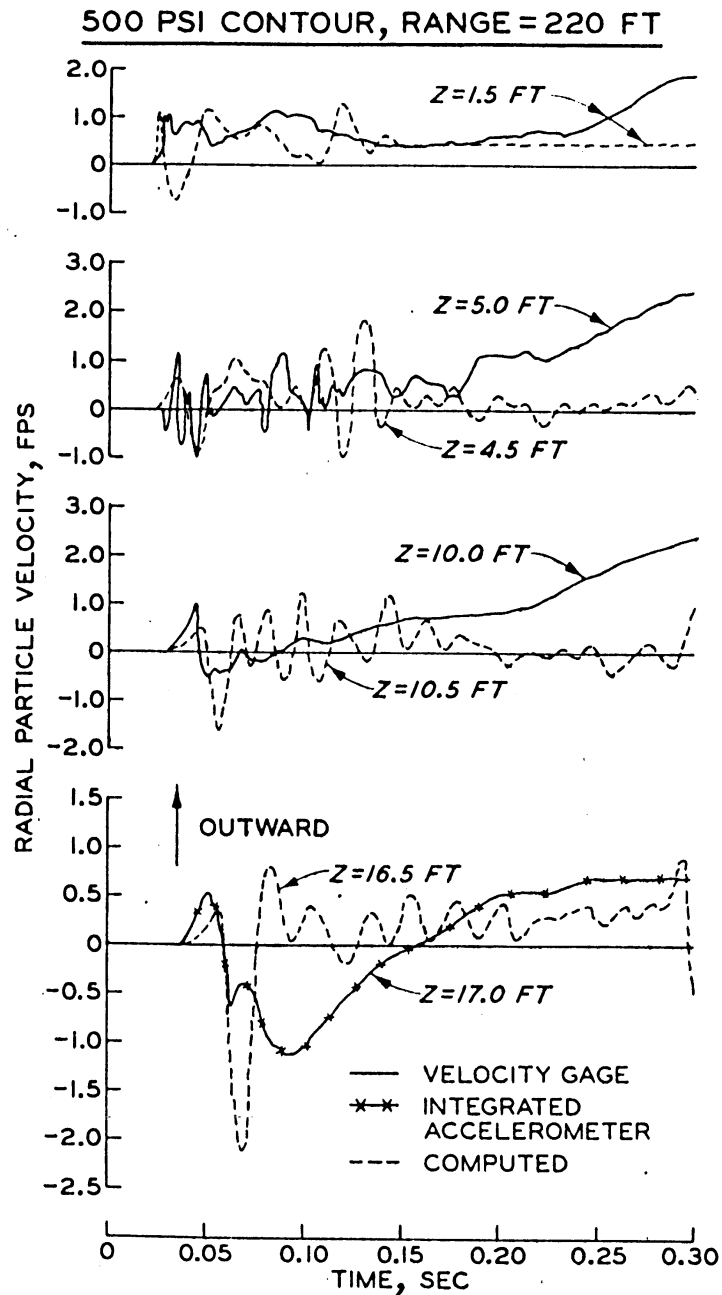


Figure 4.9 Comparison of computed radial particle velocity waveforms with field measurements; range 220 feet; Prairie Flat.

200 PSI CONTOUR, RANGE = 330 FT

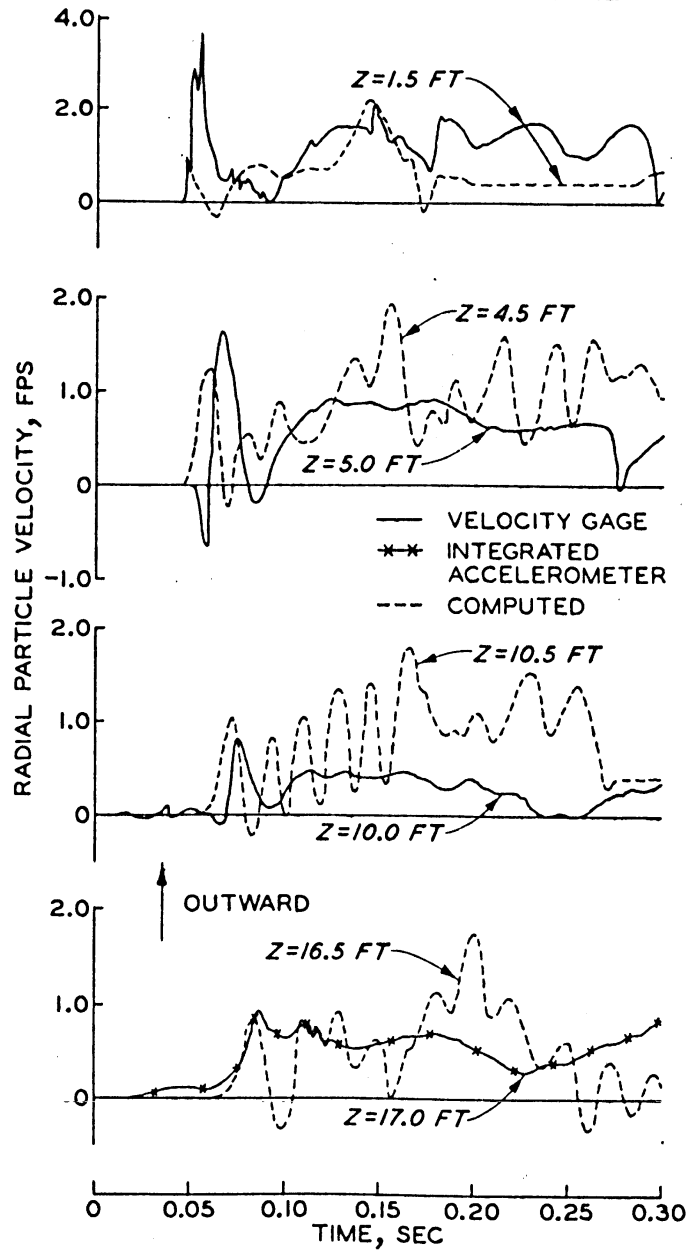


Figure 4.10 Comparison of computed radial particle velocity waveforms with field measurements; range 330 feet; Prairie Flat.

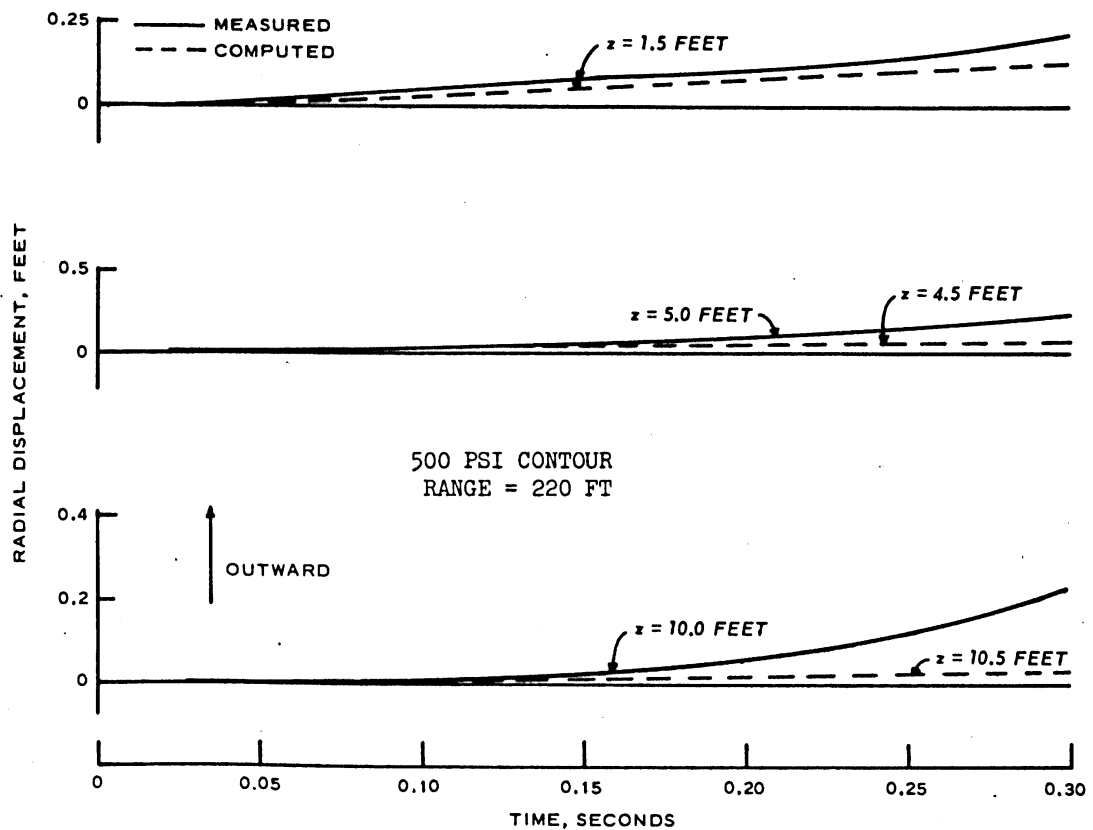


Figure 4.11 Comparison of computed radial displacement waveforms with field measurements; range 220 feet; Prairie Flat.

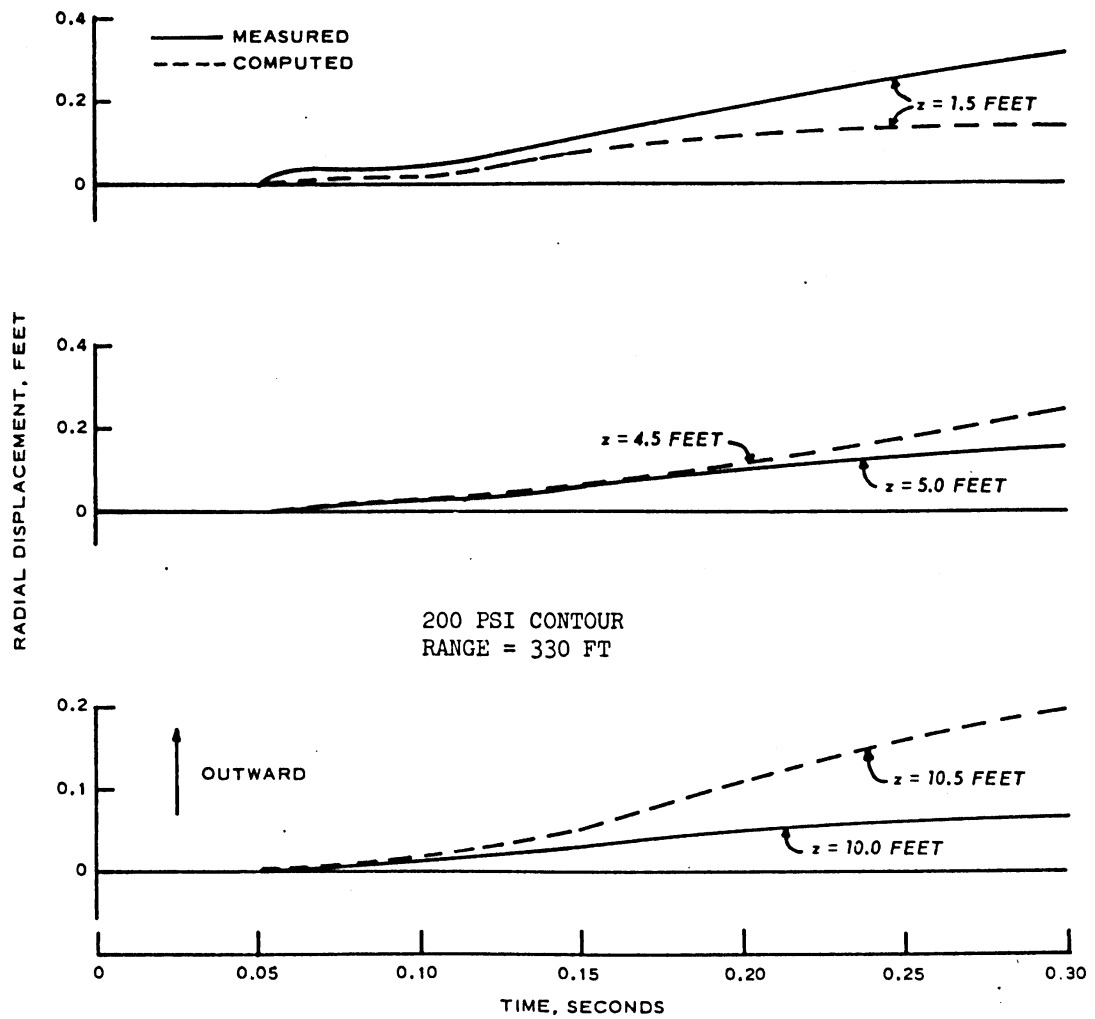


Figure 4.12 Comparison of computed radial displacement waveforms with field measurements; range 330 feet; Prairie Flat.

CHAPTER 5

CONCLUSIONS AND RECOMMENDATIONS

The major conclusion derived from this Prairie Flat analysis is that gravity effects must be included in code calculations of HE field tests conducted at the Watching Hill test range, especially if late real time ground motion phenomena are to be correctly computed. In addition, refined zoning is required in the vicinity of the ground surface to realistically predict surface peak particle velocities. These requirements are, of course, strongly dictated by the geology of this particular site and the high-intensity, short-duration nature of the overpressure pulses produced by the conventional explosives used for Watching Hill tests; however, they should be considered factors for all major ground shock calculations.

It should be readily apparent that a great deal of both quantitative and qualitative information can be extracted from a single 2D code calculation. Yet, to answer the numerous questions that come to mind concerning the effects of calculation variables such as air-blast simulation, boundary locations, grid size, layering, model coefficients, tension cutoff specifications, and gravity treatment, let alone the influences of different types of constitutive models, a large number of additional parametric calculations are required. These calculations will be performed at WES as part of the ongoing constitutive model parameter study of the Prairie Flat event. This report represents the first step in this direction.

REFERENCES

1. M. J. Dudash, ed.; "Operation PRAIRIE FLAT, Symposium Report"; DASA 2377-1 (DASIAC SR-92), Volume I, Part I, January 1970; Defense Atomic Support Agency Information and Analysis Center, General Electric, TEMPO, Santa Barbara, Calif.; Unclassified.
2. M. L. Baron, J. M. McCormick, and I. Nelson; "Investigation of Ground Shock Effects in Nonlinear Hysteretic Media"; Computational Approaches in Applied Mechanics, Preliminary Edition, ASME Computer Conference, 19-20 June 1969; Illinois Institute of Technology, Chicago, Ill., Pages 165-190; Unclassified.
3. D. C. Drucker and W. Prager; "Soil Mechanics and Plastic Analysis or Limit Design"; Quarterly of Applied Mathematics, July 1952, Volume 10, No. 2, Pages 157-165; Unclassified.
4. J. G. Jackson, Jr.; "Analysis of Laboratory Test Data to Define Soil Constitutive Properties"; Miscellaneous Paper S-69-16, April 1969; U. S. Army Engineer Waterways Experiment Station, CE, Vicksburg, Miss.; Unclassified.
5. L. Giglio-Tos; "Project LN101--Fundamental Air Blast Measurements"; DASA 2377-1 (DASIAC SR-92), Volume 1, Part I, Pages 72-109, January 1970; Defense Atomic Support Agency Information and Analysis Center, General Electric, TEMPO, Santa Barbara, Calif.; Unclassified.
6. D. W. Murrell; "Project LN302--Earth Motion and Stress Measurements"; DASA 2377-1 (DASIAC SR-92), Volume I, Part I,

Pages 242-259, January 1970; Defense Atomic Support Agency Information and Analysis Center, General Electric, TEMPO, Santa Barbara, Calif.; Unclassified.

7. R. Courant, K. Friedrichs, and M. Lewy; "Über die partiellen Differenzergleichungen der mathematischen Physik"; Math Ann., 1928, Volume 100, Pages 32-74; Unclassified.

DISTRIBUTION LIST FOR MISCELLANEOUS PAPER S-71-6

| Address | No. of Copies |
|---|---------------------|
| <u>Army</u> | |
| Chief of Engineers, Department of the Army | |
| ATTN: ENGMC-ED | 1 |
| ENGAS-I | 1 |
| Washington, D. C. 20314 | |
| Division Engineer, U. S. Army Engineer Division, Huntsville | |
| ATTN: Mr. T. R. Wathen | 1 |
| Mr. M. M. Dembo | 1 |
| P. O. Box 1600, West Station | |
| Huntsville, Ala. 35807 | |
| District Engineer, U. S. Army Engineer District, Omaha | 1 |
| 6012 U. S. Post Office and Court House | |
| 215 North 17th Street | |
| Omaha, Nebr. 68101 | |
| Director of Civil Defense, Office of the Secretary of the Army | |
| ATTN: Engineering Development Division (Research Directorate) | 1 |
| Washington, D. C. 20310 | |
| Chief of Research and Development, Department of the Army | |
| ATTN: Atomic Office | 1 |
| CRDES | 1 |
| Washington, D. C. 20310 | |
| Chief of Research and Development, Headquarters Department of the Army | 3 copies of Form |
| ATTN: Director of Army Technical Information | 1473 |
| Washington, D. C. 20310 | |
| Director, Nuclear Cratering Group | 1 |
| U. S. Army Corps of Engineer | |
| Lawrence Radiation Laboratory | |
| P. O. Box 808 | |
| Livermore, Calif. 94550 | |

| <u>Address</u> | <u>No. of Copies</u> |
|--|--------------------------|
| <u>Army (Continued)</u> | |
| Commanding Officer, U. S. Army Nuclear Defense Laboratory ATTN: Technical Library Edgewood Arsenal Edgewood, Md. 21040 | 1 |
| Director, U. S. Army Cold Regions Research and Engineering Laboratory ATTN: Mr. K. Boyd P. O. Box 282 Hanover, N. H. 03755 | 1 |
| <u>Navy</u> | |
| Commander, Naval Facilities Engineer Command Navy Department ATTN: Code 04 | 1 |
| Code 03 Washington, D. C. 20370 | 1 |
| Chief of Naval Research, Navy Department ATTN: Code 811 Washington, D. C. 20390 | 1 |
| Commanding Officer & Director U. S. Naval Civil Engineering Laboratory ATTN: Library | 1 |
| Dr. Warren A. Shaw | 1 |
| Mr. J. R. Allgood | 1 |
| Port Hueneme, Calif. 93041 | |
| <u>Air Force</u> | |
| Air Force Weapons Laboratory ATTN: Library | 2 |
| WLDC | 1 |
| Dr. H. F. Cooper, Jr. | 1 |
| CPT H. E. Selheimer | 1 |
| CPT J. C. Thompson | 1 |
| Kirtland AFB, N. Mex. 87117 | |

| <u>Address</u> | <u>No. of Copies</u> |
|---|--------------------------|
| <u>Air Force (Continued)</u> | |
| Space and Missile Systems Organization | |
| ATTN: SMQHE | 1 |
| SMQHF-1 | 1 |
| Norton AFB, Calif. 92409 | |
| Director of Civil Engineering, Headquarters, USAF | 1 |
| ATTN: AFOCE | |
| Washington, D. C. 20330 | |
| Director, U. S. Air Force Project RAND | |
| Via: U. S. Air Force Liaison Office | |
| The Rand Corporation | |
| 1700 Main Street | |
| ATTN: Library | 1 |
| Dr. Harold Brode | 1 |
| Santa Monica, Calif. 90406 | |
| <u>Colleges and Universities</u> | |
| University of California, Lawrence Radiation Laboratory | 1 |
| P. O. Box 808 | |
| ATTN: Technical Information Division | |
| Livermore, Calif. 94550 | |
| City College of New York, Department of Civil Engineering | 1 |
| ATTN: Dr. C. J. Costantino | |
| New York, N. Y. 10010 | |
| Duke University, Department of Civil Engineering | 1 |
| ATTN: Professor Aleksander B. Vesic | |
| Durham, N. C. 27706 | |
| The George Washington University | 1 |
| ATTN: Professor Raymond R. Fox | |
| Nuclear Defense Design Center | |
| School of Engineering and Applied Science | |
| Washington, D. C. 20006 | |

| Address | No. of Copies |
|---|------------------|
| <u>Colleges and Universities (Continued)</u> | |
| Georgia Institute of Technology, School of Civil Engineering ATTN: Dr. B. B. Mazanti Atlanta, Ga. 30332 | 1 |
| Howard University, Department of Civil Engineering ATTN: Dr. Delon Hampton Washington, D. C. 20001 | 1 |
| University of Illinois, Department of Civil Engineering ATTN: Professor A. H. S. Ang | 1 |
| Professor A. J. Hendron, Jr. | 1 |
| Professor N. M. Newmark | 1 |
| Urbana Campus Urbana, Ill. 61801 | |
| Louisiana State University, Department of Civil Engineering ATTN: Dr. J. K. Poplin Baton Rouge, La. 70803 | 1 |
| The University of Michigan, Department of Civil Engineering ATTN: Professor F. E. Richart, Jr. Ann Arbor, Mich. 48104 | 1 |
| University of New Mexico, Civil Engineering Research Facility ATTN: Mr. Delmar E. Calhoun | 1 |
| Dr. G. Triandafilidis | 1 |
| P. O. Box 188, University Station Albuquerque, N. Mex. 87106 | |
| State University of New York, Department of Civil Engineering ATTN: Dr. Ernest T. Selig Buffalo, N. Y. 14214 | 1 |
| University of Utah ATTN: Dr. Wayne Brown Department of Mechanical Engineering Salt Lake City, Utah 84112 | 1 |

| <u>Address</u> | <u>No. of Copies</u> |
|---|--------------------------|
| <u>Colleges and Universities (Continued)</u> | |
| Massachusetts Institute of Technology, Division of Sponsored Research ATTN: Dr. Robert V. Whitman 77 Massachusetts Avenue Cambridge, Mass. 02139 | 1 |
| California Institute of Technology, Division of Engineering ATTN: Dr. Ronald Scott Pasadena, Calif. 91109 | 1 |
| University of California ATTN: Professor H. Bolton Seed Room 301, Engineering Materials Laboratory Berkeley, Calif. 94720 | 1 |
| Texas A&M University, Department of Civil Engineering ATTN: Professor L. J. Thompson Professor W. A. Dunlap Professor J. Hardin College Station, Tex. 77843 | 1 1 1 |
| Brown University Division of Engineering ATTN: Dr. W. Prager Providence, R. I. 02912 | 1 |
| George Washington University Department of Engineering Mechanics ATTN: Dr. A. Freudenthal Washington, D. C. 20006 | 1 |
| <u>Other</u> | |
| Agbabian-Jacobsen Associates, Engineering Consultants 8939 South Sepulveda Boulevard Los Angeles, Calif. 90045 | 1 |

| Address | No. of Copies |
|---|------------------|
| <u>Other (Continued)</u> | |
| Applied Theory Incorporated ATTN: Dr. John G. Trulio Mr. W. J. Niles 1010 Westwood Boulevard Los Angeles, Calif. 90024 | 1 1 |
| Battelle Memorial Institute ATTN: Dr. P. N. Lamori 505 King Avenue Columbus, Ohio 43201 | 1 |
| The Boeing Company, Aerospace Group Missile and Information Systems Division ATTN: Mr. Robert W. Hager Mr. H. G. Leistner Mr. Ken Levien Mr. Joel K. Bloomer P. O. Box 3985 Seattle, Wash. 98124 | 1 1 1 1 |
| Director, Defense Atomic Support Agency ATTN: SPSS Washington, D. C. 20301 | 5 |
| Defense Documentation Center (DDC) ATTN: Mr. Myer Kahn Cameron Station Alexandria, Va. 22314 (NO TOP SECRET TO THIS ADDRESS) | 12 |
| Director, Defense Intelligence Agency ATTN: DIAAP-1K2 Washington, D. C. 20301 | 1 |
| Director of Defense Research and Engineering ATTN: Technical Library Washington, D. C. 20301 | 1 |
| Defence Research Establishment, Suffield Ralston, Alberta, Canada | 1 |

| <u>Address</u> | <u>No. of Copies</u> |
|--|--------------------------|
| <u>Other (Continued)</u> | |
| Denver Mining Research Center ATTN: Dr. Leonard A. Obert Building 20, Denver Federal Center Denver, Colo. 80225 | 1 |
| Mr. John Foss, Outside Structures Department Bell Telephone Laboratories Whippany, N. J. 07981 | 1 |
| General American Transportation Corporation General American Research Division ATTN: Dr. G. L. Neidhardt 7449 North Natchez Avenue Niles, Ill. 60648 | 1 |
| General Motors Corporation, Manufacturing Development ATTN: Mr. W. M. Isbell Technical Center Warren, Mich. 48090 | 1 |
| Dr. Robert L. Kondner KONDNER RESEARCH Downes Road Parkton, Md. 21120 | 1 |
| Los Alamos Scientific Laboratory P. O. Box 1663 ATTN: Report Librarian Los Alamos, N. Mex. 87544 | 1 |
| Mr. W. R. Perret 5112 Sandia Laboratories Sandia Base Albuquerque, N. Mex. 87115 | 1 |
| Sandia Laboratories ATTN: Classified Document Division for Dr. M. L. Merritt P. O. Box 5800 Albuquerque, N. Mex. 87115 | 1 |

| Address | No. of Copies |
|--|------------------|
| <u>Other (Continued)</u> | |
| Systems, Science & Software ATTN: Mr. Robert T. Allen P. O. Box 1620 La Jolla, Calif. 92037 | 1 |
| Shock Hydrodynamics, Inc. 15010 Ventura Boulevard Sherman Oaks, Calif. 91403 | 1 |
| Commander, Test Command, Defense Atomic Support Agency ATTN: TCCOM, TCDT Sandia Base Albuquerque, N. Mex. 87115 | 1 |
| Physics International Company ATTN: Dr. Charles Godfrey Mr. Fred M. Sauer 2700 Merced Street San Leandro, Calif. 94577 | 1 1 |
| TRW Systems ATTN: Dr. Peter Dai Mr. Norman Lipner One Space Park Redondo Beach, Calif. 90278 | 1 1 |
| TRW Systems ATTN: Mr. Fred A. Pieper P. O. Box 1310 San Bernardino, Calif. 92402 | 1 |
| Paul Weidlinger, Consulting Engineer ATTN: Dr. M. L. Baron Dr. Ivan Nelson 110 East 59th Street New York, N. Y. 10022 | 1 1 |
| Mr. G. F. Weissmann Room 1B-124, Bell Telephone Laboratories Murray Hill, N. J. 07971 | 1 |

| <u>Address</u> | <u>No. of Copies</u> |
|---|--------------------------|
| <u>Other (Continued)</u> | |
| Shannon and Wilson, Inc. ATTN: Mr. Earl A. Sibley 1105 North 38th Street Seattle, Wash. 98103 | 1 |
| Director, Advanced Research Projects Agency ATTN: Dr. Stanley Ruby (NMRO-RM. 3D170) The Pentagon Washington, D. C. 20315 | 1 |
| Aerospace Corporation ATTN: Dr. S. B. Batdorf | 1 |
| Dr. M. B. Watson 1111 E. Mill Street San Bernardino, Calif. 92408 | 1 |

Unclassified

Security Classification

| DOCUMENT CONTROL DATA - R & D | | |
|---|---|--|
| (Security classification of title, body of abstract and indexing annotation must be entered when the overall report is classified) | | |
| 1. ORIGINATING ACTIVITY (Corporate author) U. S. Army Engineer Waterways Experiment Station Vicksburg, Mississippi | | 2a. REPORT SECURITY CLASSIFICATION Unclassified |
| | | 2b. GROUP |
| 3. REPORT TITLE FREE-FIELD CODE PREDICTIONS VERSUS FIELD MEASUREMENTS: A COMPARATIVE ANALYSIS FOR THE PRAIRIE FLAT EVENT | | |
| 4. DESCRIPTIVE NOTES (Type of report and inclusive dates) Final report | | |
| 5. AUTHOR(S) (First name, middle initial, last name) Joseph S. Zelasko George Y. Baladi | | |
| 6. REPORT DATE March 1971 | 7a. TOTAL NO. OF PAGES 74 | 7b. NO. OF REFS 7 |
| 8a. CONTRACT OR GRANT NO. | 8b. ORIGINATOR'S REPORT NUMBER(S) Miscellaneous Paper S-71-6 | |
| b. PROJECT NO. | | |
| c. Subtask SB209 | 9b. OTHER REPORT NO(S) (Any other numbers that may be assigned this report) | |
| d. | | |
| 10. DISTRIBUTION STATEMENT This document has been approved for public release and sale; its distribution is unlimited. | | |
| 11. SUPPLEMENTARY NOTES Paper presented at Eric C. Wang Symposium on Protective Structures Technology, Air Force Weapons Laboratory, Kirtland AFB, N. Mex., 21-23 July 1970. | | 12. SPONSORING MILITARY ACTIVITY Defense Atomic Support Agency Washington, D. C. |
| 13. ABSTRACT This report documents the results of an airblast-induced ground-shock calculation performed at the U. S. Army Engineer Waterways Experiment Station (WES) for the Operation Prairie Flat 500-ton high-explosive (HE) event. A WES-modified version of the 2D axisymmetric LAYER Code developed by the Paul Weidlinger firm was used for the investigation. Each layer of the soil profile was mathematically modeled with a nonlinear elastic-plastic-compacting type constitutive model that provided good fits to the available material property test data. Field airblast measurements were used to develop an airblast routine suitable for code input. The code results, carried to 300 msec of real time, showed good quantitative and qualitative agreement with the field ground-motion measurements in regions outside the crater zone. The calculations reported herein represent initial efforts at WES to conduct comprehensive parametric studies of the effectiveness of contemporary mathematical constitutive models in predicting airblast-induced ground motions for several high-explosive field tests. The overall research program includes study of the influences of computational details such as boundary conditions, grid size, and time step and comparative analyses of the calculated ground motions and those recorded during the field test events. | | |

DD FORM 1473

REPLACES DD FORM 1473, 1 JAN 64, WHICH IS OBSOLETE FOR ARMY USE.

Unclassified

Security Classification

Unclassified
Security Classification

| 14. KEY WORDS | LINK A | | LINK B | | LINK C | |
|--------------------------|--------|----|--------|----|--------|----|
| | ROLE | WT | ROLE | WT | ROLE | WT |
| Airblast waves | | | | | | |
| Code predictions | | | | | | |
| Explosion effects | | | | | | |
| Ground motion | | | | | | |
| Ground shock | | | | | | |
| Mathematical models | | | | | | |
| Prairie Flat (Operation) | | | | | | |